

Spirit Mars Rover Mission: Overview and selected results from the northern Home Plate Winter Haven to the side of Scamander crater

R. E. Arvidson,¹ J. F. Bell III,² P. Bellutta,³ N. A. Cabrol,^{4,5} J. G. Catalano,¹ J. Cohen,⁶ L. S. Crumpler,⁷ D. J. Des Marais,⁴ T. A. Estlin,³ W. H. Farrand,⁸ R. Gellert,⁹ J. A. Grant,¹⁰ R. N. Greenberger,¹ E. A. Guinness,¹ K. E. Herkenhoff,¹¹ J. A. Herman,³ K. D. Iagnemma,¹² J. R. Johnson,¹¹ G. Klingelhöfer,¹³ R. Li,¹⁴ K. A. Lichtenberg,¹ S. A. Maxwell,³ D. W. Ming,¹⁵ R. V. Morris,¹⁵ M. S. Rice,² S. W. Ruff,¹⁶ A. Shaw,¹ K. L. Siebach,¹ P. A. de Souza,¹⁷ A. W. Stroupe,³ S. W. Squyres,² R. J. Sullivan,² K. P. Talley,³ J. A. Townsend,³ A. Wang,¹ J. R. Wright,³ and A. S. Yen³

Received 23 April 2010; revised 6 June 2010; accepted 15 June 2010; published 30 September 2010.

[1] This paper summarizes Spirit Rover operations in the Columbia Hills, Gusev crater, from sol 1410 (start of the third winter campaign) to sol 2169 (when extrication attempts from Troy stopped to winterize the vehicle) and provides an overview of key scientific results. The third winter campaign took advantage of parking on the northern slope of Home Plate to tilt the vehicle to track the sun and thus survive the winter season. With the onset of the spring season, Spirit began circumnavigating Home Plate on the way to volcanic constructs located to the south. Silica-rich nodular rocks were discovered in the valley to the north of Home Plate. The inoperative right front wheel drive actuator made climbing soil-covered slopes problematical and led to high slip conditions and extensive excavation of subsurface soils. This situation led to embedding of Spirit on the side of a shallow, 8 m wide crater in Troy, located in the valley to the west of Home Plate. Examination of the materials exposed during embedding showed that Spirit broke through a thin sulfate-rich soil crust and became embedded in an underlying mix of sulfate and basaltic sands. The nature of the crust is consistent with dissolution and precipitation in the presence of soil water within a few centimeters of the surface. The observation that sulfate-rich deposits in Troy and elsewhere in the Columbia Hills are just beneath the surface implies that these processes have operated on a continuing basis on Mars as landforms have been shaped by erosion and deposition.

Citation: Arvidson, R. E., et al. (2010), Spirit Mars Rover Mission: Overview and selected results from the northern Home Plate Winter Haven to the side of Scamander crater, *J. Geophys. Res.*, 115, E00F03, doi:10.1029/2010JE003633.

¹Department of Earth and Planetary Sciences, Washington University in St. Louis, St. Louis, Missouri, USA.

²Department of Astronomy, Cornell University, Ithaca, New York, USA.

³Jet Propulsion Laboratory, California Institute of Technology, Pasadena, California, USA.

⁴NASA Ames Research Center, Moffett Field, California, USA.

⁵SETI Institute, Mountain View, California, USA.

⁶Honeybee Robotics Spacecraft Mechanisms Corporation, New York, New York, USA.

⁷New Mexico Museum of Natural History and Science, Albuquerque, New Mexico, USA.

⁸Space Science Institute, Boulder, Colorado, USA.

⁹Department of Physics, University of Guelph, Guelph, Ontario, Canada.

¹⁰Center for Earth and Planetary Studies, Smithsonian Institution, Washington, DC, USA.

1. Introduction

[2] The Mars Exploration Rover, Spirit, touched down on the volcanic plains of Gusev Crater on 4 January 2004. Since landing, Spirit has conducted numerous traverses and made extensive measurements on the plains that dominate the floor of the crater and the soil-covered and rocky sur-

¹¹U.S. Geological Survey, Flagstaff, Arizona, USA.

¹²Department of Mechanical Engineering, Massachusetts Institute of Technology, Cambridge, Massachusetts, USA.

¹³Institut für Anorganische und Analytische Chemie, Johannes Gutenberg-Universität, Mainz, Germany.

¹⁴Department of Civil and Environmental Engineering and Geodetic Science, Ohio State University, Columbus, Ohio, USA.

¹⁵NASA Johnson Space Center, Houston, Texas, USA.

¹⁶School of Earth and Space Exploration, Arizona State University, Tempe, Arizona, USA.

¹⁷Information and Communication Technologies Centre, CSIRO, Hobart, Tasmania, Australia.

Table 1. Spirit's Payload Elements^a

Instrument	Key Parameters
<i>Mast-Mounted Science Instruments</i>	
Pancam: Panoramic Camera	Multispectral imager (0.4 to 1.0 μm) with stereoscopic capability; 0.28 mrad IFOV; 16.8° by 16.8° FOV. Stereo baseline separation of 30 cm. External calibration target on rover deck.
MiniTES: Thermal Emission Spectrometer	Emission spectra (5 to 29 μm , 10 cm^{-1} resolution) with 8 or 20 mrad FOV. Internal and external blackbody calibration targets.
<i>IDD-Mounted In Situ Package</i>	
APXS: Alpha Particle X-Ray Spectrometer	²⁴⁴ Cm alpha particle sources, and X-ray detectors, 3.8 cm FOV.
MB: Mössbauer Spectrometer	⁵⁷ Fe spectrometer in backscatter mode; ⁵⁷ Co/Rh source and Si-PIN diode detectors; field of view approximately 1.5 cm^2 .
MI: Microscopic Imager	31 $\mu\text{m}/\text{pixel}$ monochromatic imager (1024x1024) with 2 mm depth of field.
RAT: Rock Abrasion Tool	Tool originally capable of preparing 5 mm deep by 4.5 cm wide surface on rocks. For period covered in this paper: Grinding bit pads were worn away by sol 416 and RAT primarily used for rock brushing. Implemented soil “grind” at Troy using steel pieces that held bit pads in place. Encoder for grind motor stopped working on sol 1341 thus replaced seek/scan with “grind scan” that started from the Z home position and implemented large steps with grind motor run at low voltage to stall when RAT hit surfaces.
<i>Engineering Cameras</i>	
Navigation Cameras (Navcam)	Mast-mounted panchromatic stereoscopic imaging system with 0.77 mrad IFOV; 45° FOV, and 20 cm stereo baseline separation.
Hazard Avoidance Cameras (Hazcam)	Front and rear-looking panchromatic stereoscopic imaging systems with 2 mrad IFOV; 123° FOV, 10 cm stereo baseline separation.

^aMagnets were also included on the spacecraft but not described.

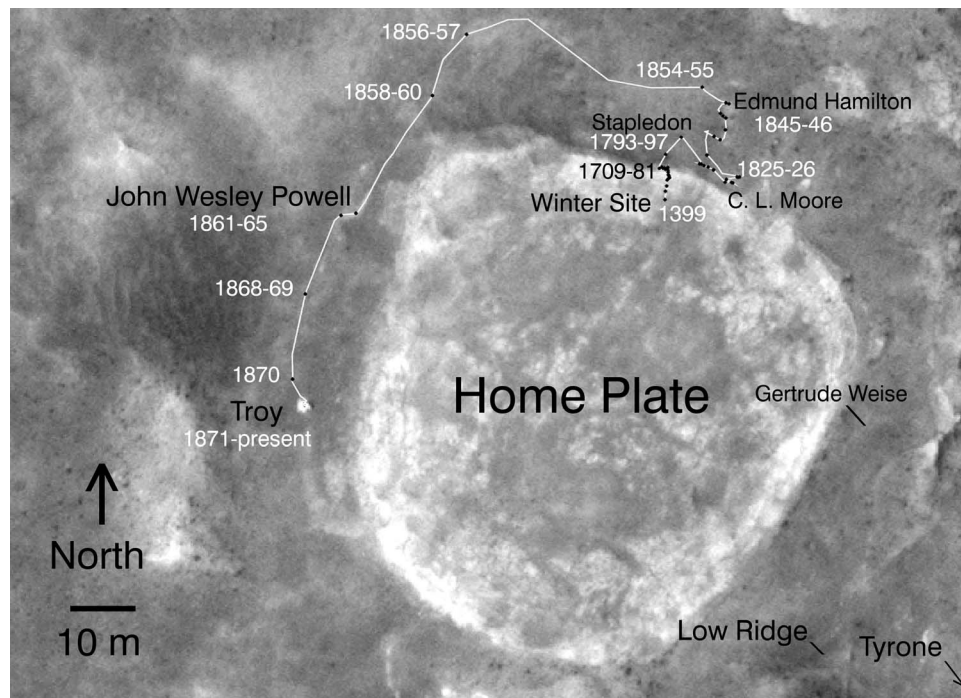


Figure 1. HiRISE subframe showing Home Plate with sites and traverses overlain since the third winter campaign site on the northern slopes of Home Plate to embedding of Spirit at Troy. Times in sols for selected locations are shown, along with place names for areas highlighted in this paper. Spirit is the white feature located in Troy. The area called the sidewalk is located to the southeast of Spirit. Low Ridge is where Spirit spent its second winter; Tyrone is the location (off to lower right beyond image coverage) of sulfate-bearing soils, and Gertrude Weise is the location of opaline silica deposits investigated by Spirit. HiRISE image ESP_0013499_1650_red.

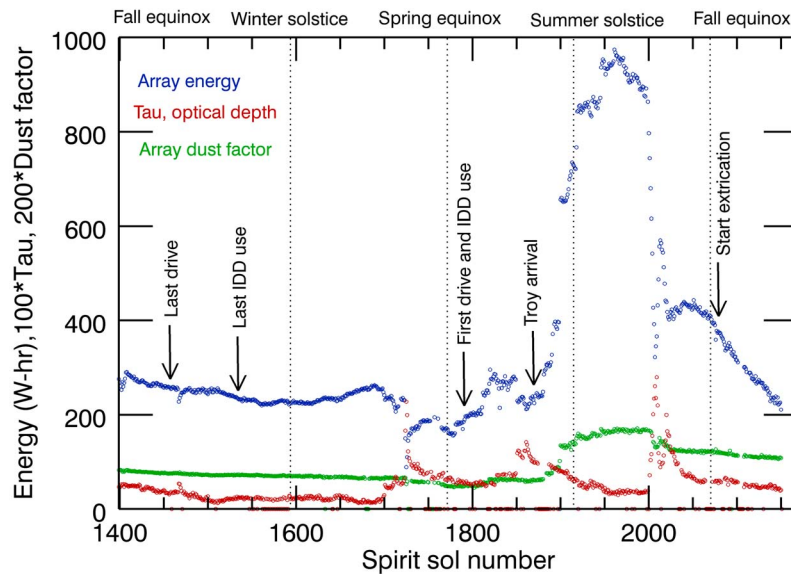


Figure 2. Timeline of events, including atmospheric optical depth, solar array energy, dust loading on the array, seasons, and key activities for Spirit covering the period from when Spirit wintered on the northern slopes of Home Plate to when Troy extrication drives stopped (sol 2165) because of the onset of the fourth winter season. The first drive downhill from the third winter site occurred on sol 1772, followed closely by acquisition of in situ data for the target Stapledon (Figure 3). A series of solar array dust cleaning events coincided with the onset of the summer season while Spirit was embedded in Troy sandy materials.

faces within the older Columbia Hills (see *Arvidson et al.* [2006] and [2008] for mission summaries and science highlights and Table 1 for payload description). The purpose of this paper is to summarize operations and present scientific highlights from the time Spirit began its third winter campaign on the north side of Home Plate on sol 1410 to the start of its fourth winter stay on sol 2169 on the side of a crater informally named Scamander. This crater is located in the valley to the west of Home Plate (Figures 1–2 and Table 2).

[3] Spirit’s right front wheel drive actuator failed on sol 779 and was declared inoperative on sol 787 [*Arvidson et al.*, 2008]. Driving up soil-covered slopes with tilts more than several degrees has proven to be problematic and led to significant wheel slippage, sinkage, and exposure of subsurface soils, culminating in embedding in soils in Troy (Figure 1). On the other hand, measurements of the soils excavated during drives have provided new insights into the aqueous history of the Inner Basin around Home Plate and are the key science highlight presented in this paper. This overview of operations and scientific results is meant to complement papers that provide detailed findings about the geology, chemistry, and mineralogy of Husband Hill and the Inner Basin that are included as the fourth set of Mars Exploration Rover papers published in the *Journal of Geophysical Research*.

2. Five Wheel Drive Dynamics

[4] As noted in section 1, Spirit’s right front wheel drive actuator failed relatively early during the mission. The wheels were designed with permanent magnetic detents to keep them from rolling (e.g., downhill) when not actuated. This

detent-induced resisting stress for the inoperative right front wheel typically exceeded the soil shear strength during drives, causing soil failure and exposing subsurface soils (e.g., Figure 3). The drag stress also caused the vehicle to yaw counterclockwise (viewed from above) when driving backward and clockwise when driving forward. To better understand the dynamics associated with these motions, a two hundred element rigid body software model of the rover developed by *Lindemann and Voorhees* [2005] was utilized to calculate forces and torques associated with five- and six-wheel driving across flat surfaces and slopes covered by soils. The simulations assume a simplified model of wheel-soil interactions that is dominated by frictional stresses using Coulomb parameters for static and dynamic coefficients of friction.

[5] Specifically, drives were simulated in which the maximum shear stress, $F_{s,max}$, that could be exerted by a wheel on the soil before failure was set to the soil Coulomb shear strength:

$$F_{s,max} = C + F_n \tan \Phi$$

where C is the soil cohesion, F_n is the normal stress due to the weight of the rover on the wheel, Φ is the soil angle of internal friction, and $\tan \Phi$ is static coefficient of friction. Values for cohesion and angle of internal friction (i.e., to determine the effective static coefficient of friction) of 1 to 5 kPa and 30 degrees, respectively, were used in the computations. These values are similar to those retrieved from trenching experiments conducted on the Gusev plains by R. J. Sullivan et al. (Cohesions, friction angles, and other physical properties of Martian regolith from MER wheel trenches and wheel scuffs, submitted to *Journal of Geophysical Research*,

Table 2. Major Activities for Spirit Organized by Sol^a

Earth Date	Sol	Activity	Site
12/17/07–12/15/08	1410–1760	Winter campaign: IDD measurements of Chanute, Freeman, Wendell Pruitt rock targets, Arthur C. Harmon soil target and magnets; Tuskegee Pancam panorama; atmospheric RS	133–135
2/27/08–10/19/09	1476–1705	Pancam 13F “Bonestell” Panorama	134
3/26/2008	1503	Pancam superres “Roger_Zellazny” target	134
4/2/08–4/25/08	1510–1532	MI, APXS, MB “Arthur_C_Harmon” soil target	134
4/4/2008	1512	Pancam superres “Arthur_C_Clarke”	134
5/14/08–10/6/08	1551–1692	IDD in winter hibernation position	134
10/23/08–11/8/08	1709–1724	Drive uphill to follow the sun	134–135
11/30/08–12/15/08	1746–1760	Solar Conjunction	135
12/16/08–12/17/08	1761–1762	RS and Health Check	135
12/18/08–12/23/08	1763–1768	Attempt to drive uphill out of winter position	135
12/14/08–12/26/08	1769–1771	Atmospheric RS	135
12/27/2008	1772	Attempt to drive downhill out of winter position	135
12/28/08–12/29/08	1773–1774	Atmospheric RS	135
12/30/08–1/1/09	1775–1777	Runout	135
1/2/09–1/5/09	1778–1781	Automode	135
1/6/2009	1782	Drive downhill out of winter position	135
1/8/09–1/14/09	1783–1789	RS surroundings; Pancam superres “Jack Williamson”	135
1/15/09–1/17/09	1790–1792	Runout	135
1/18/2009	1793	Drive to “Stapledon”	135
1/19/09–1/20/09	1794–1795	RS; Pancam 13F “Thunderbolt”	135
1/21/2009	1796	MI, APXS “Stapledon” target	135
1/22/2009	1797	RS surroundings	135
1/23/2009	1798	Drive toward “Home Plate” on ramp	135
1/24/09–1/30/09	1799–1805	Atmospheric RS	135
1/31/09–2/12/09	1806–1818	Attempt to drive onto “Home Plate”; Atmospheric RS; excavated disturbed soil “C. L. Moore”	135
2/14/2009	1819	Atmospheric RS	135
2/15/2009	1820	Extrication from soft material	135
2/16/09–2/23/09	1821–1828	Attempt to drive uphill onto “Home Plate”; Atmospheric RS	135
2/24/09–3/10/09	1829–1843	Attempt to drive to NE corner of “Home Plate”; Excavated disturbed soil “Edmund Hamilton”	135–136
3/11/09–3/21/09	1844–1854	Attempt to drive toward NW corner of “Home Plate”; Targeted and Atmospheric RS	136
3/22/09–3/29/09	1855–1861	Drive west around “Home Plate”; RS	136
3/30/2009	1862	Atmospheric RS	136
3/31/09–4/2/09	1863–1865	MI, APXS, “John Wesley Powell”; Pancam 8F “Pioneer”	136
4/3/2009	1866	Pancam 13F “John Wesley Powell”; Drive South	136
4/4/2009	1867	Pancam 13F “York”	136
4/5/09–4/8/09	1868–1871	Drive into “West Valley”; RS	136–137
4/9/09–4/20/09	1872–1885	Automode and Earth control	137
4/21/09–5/7/09	1886–1899	Attempts to drive South in West Valley and out of embedded position	137
5/8/09–5/24/09	1900–1916	Mobility diagnostics; RS	137
5/18/09–6/12/09	1910–1934	Calypso Panorama	137
5/25/09–5/29/09	1917–1921	RS surroundings	137
5/30/09–6/1/09	1922–1924	MI, MB “Sackrider”	137
6/2/09–6/3/09	1925–1926	MI, APXS “Sackrider”	137
6/4/2009	1927	MI “Olive tree”; MI, APXS “Olive Branch1”	137
6/5/09–6/10/09	1928–1932	APXS, MI, MB “Olive Branch2”	137
6/11/2009	1933	Left middle wheel diagnostics	137
6/12/2009	1934	MI, APXS “Olive Branch3”	137
6/13/2009	1935	MI, APXS “Olive Branch4”	137
6/12/09–7/8/09	1934–1960	Twilight observations	137
6/14/09–6/17/09	1936–1939	MI, MB, APXS, Pancam “Penina1”	137
6/18/2009	1940	MI, APXS “Penina2”	137
6/19/2009	1941	MI, APXS “Penina3”	137
6/20/09–6/22/09	1942–1944	MB “Penina1”	137
6/23/2009	1945	MI, APXS and RS “Cyclops Eye_a” undisturbed soil target	137
6/24/2009	1946	MI, APXS and RS “Cyclops Eye2” undisturbed soil target	137
6/25/09–6/29/09	1947–1951	MI, APXS, MB “Cyclops Eye3” undisturbed soil target	137
6/30/2009	1952	RAT Grind Scan; RS “Cyclops Eye3”	137
7/1/09–7/13/09	1953–1964	Atmospheric RS; APXS Argon	137
7/7/09–7/13/09	1959–1964	Targeted RS and superresolution imaging	137
7/12/2009	1963	RAT Grind Scan; MI, Pancam “Cyclops Eye3”	137
7/14/2009	1965	RAT Brush “Cyclops Eye3”	137
7/15/09–7/20/09	1966–1971	MI, APXS, MB, Pancam “Cyclops Eye4”	137
7/16/2009	1967	MI, APXS “Olive Branch5”	137
7/17/09–7/24/09	1968–1975	Navcam illumination experiment	137
7/21/2009	1972	RAT Grind Scan “Cyclops Eye4”; APXS Argon	137
7/22/2009	1973	Attempt to RAT grind “Cyclops Eye4” failed; APXS, Pancam “Cyclops Eye5”	137

Table 2. (continued)

Earth Date	Sol	Activity	Site
7/23/2009	1974	Runout	137
7/24/2009	1975	MI “Olive Branch6”; MI “Cyclops Eye5”	137
7/25/09–7/27/09	1976–1978	Targeted and atmospheric RS; Pancam 13F tracks, “Cyclops Eye5”	137
7/28/2009	1979	MI, APXS “Olive Pit”	137
7/29/2009	1980	MI, APXS “Polyphemus Eye1”; RAT grind scan	137
7/30/2009	1981	RAT Grind at “Polyphemus Eye1”; MI, APXS “Polyphemus Eye2”	137
7/31/2009	1982	MI “Sackrider”; Pancam 13F “Polyphemus Eye2”	137
7/31/09–8/3/09	1982–1985	MB “Cyclops Eye5” disturbed soil target; RS	137
8/4/2009	1986	RAT grind scan; MI “Penina2”; RS	137
8/5/2009	1987	Pancam 13F right track	137
8/6/09–8/7/09	1988–1989	MRO safe mode; Runout	137
8/8/2009	1990	MI rover undercarriage; RAT grind (unsuccessful), MI, Pancam “Cyclops Eye6”	137
8/9/09–8/10/09	1991–1992	Atmospheric RS	137
8/11/2009	1993	RAT grind scan “Polyphemus Eye2” disturbed soil target; APXS Argon	137
8/12/2009	1994	APXS Argon; RS	137
8/13/09–8/14/09	1995–1996	RAT Grind, MI, APXS, MB “Polyphemus Eye3” disturbed soil target; RS	137
8/15/2009	1997	MI, APXS “Olive Leaf” target; RS	137
8/16/09–8/24/09	1998–2005	MB, Pancam “Polyphemus Eye3”	137
8/25/2009	2006	RAT penetrometer experiment (“Ulysses Spear”)	137
8/26/2009	2007	MB “Olive Leaf”; Pancam left middle wheel	137
8/27/2009	2008	Atmospheric RS; Pancam left middle wheel	137
8/28/2009	2009	Runout	137
8/29/09–8/30/09	2010–2011	MB “Olive Leaf” target; Pancam 13F “Scamander Plains”	137
8/31/2009	2012	Atmospheric RS; Pancam right middle wheel; Pancam 13F “Scamander Plains”	137
9/1/2009	2013	Runout	137
9/2/2009–9/3/09	2014–2015	MB “Olive Leaf” target; Pancam 13F “Scamander Plains”	137
9/4/2009	2016	APXS “Olive Leaf”; Pancam 13F “Scamander Plains”	137
9/5/09–9/11/09	2017–2023	APXS Integration on capture magnet; Pancam 13F work volume and “Scamander Plains”	137
9/12/2009	2024	MI rover undercarriage; MI and APXS “Penina4”	137
9/13/09–9/16/09	2025–2028	MB “Penina4”	137
9/17/09–9/21/09	2029–2033	Atmospheric RS	137
9/22/09–9/24/09	2034–2035	Automode	137
9/25/09–9/26/09	2036–2037	Atmospheric RS; APXS Argon	137
9/27/09–9/28/09	2038–2039	Runout	137
9/29/09–9/30/09	2040–2041	Atmospheric RS	137
10/1/2009	2042	Runout	137
10/2/2009	2043	Atmospheric RS	137
10/3/2009	2044	MI Rover undercarriage; MI, MB “Stratius”	137
10/4/2009–10/5/09	2045–2046	MB “Stratius”	137
10/6/2009	2047	Runout	137
10/7/2009	2048	MB “Stratius”	137
10/8/2009–10/10/09	2049–2051	APXS “Stratius”; Pancam 13F “Scamander Plains”	137
10/11/2009	2052	MI, MB “Thoosa”; Pancam 13F “Scamander Plains”	137
10/12/09–10/15/09	2053–2056	Runout	137
10/16/09–10/21/09	2057–2062	MB “Thoosa”; Pancam 13F “Scamander Plains”	137
10/20/2009	2061	MI rover undercarriage	137
10/22/2009	2063	MB “Thoosa”	137
10/23/2009	2064	MB “Thoosa”; Pancam 13F “Scamander Plains”	137
10/24/09–10/28/09	2065–2069	Safe mode and recovery	137
10/29/09–10/30–09	2070–2071	APXS “Thoosa”	137
11/1/2009	2072	MI “BellyRock”	138
11/2/09–11/3/09	2073–2074	Engineering only, prep for flash reformat	138
11/4/2009	2075	Reformat flash; MI “BellyRock”	138
11/5/2009	2076	MI Shoulder Joint	138
11/6/2009	2077	Atmospheric RS	138
11/7/09–11/9/09	2078–2080	Straighten wheels for drive; Pancam 13F “Scamander Plains”	138
11/10/09	2081	MI “BellyRock”	138
11/11/2009–11/16/09	2082–2087	Atmospheric RS; Pancam 13F “Scamander Plains”	138
11/17/09	2088	Troy Extraction Attempt; MI “BellyRock”	138
11/18/09	2089	Pancam 13F “Scamander Plains”	138
11/19/09	2090	Troy Extraction Attempt; MI “BellyRock”	138
11/20/09	2091	Atmospheric RS	138
11/21/09	2092	Troy Extraction Attempt; MI “BellyRock”	138
11/22/09–11/23/09	2093–2094	Atmospheric RS	138
11/24/09	2095	Troy Extraction Attempt; MI “BellyRock”	138
11/25/09–11/27/09	2096–2098	Atmospheric RS	138
11/28/09	2099	Troy Extraction Attempt; MI “BellyRock”	138
11/29/09–11/30/09	2100–2101	Atmospheric RS	138
12/1/09	2102	Pancam Magnets	138

Table 2. (continued)

Earth Date	Sol	Activity	Site
12/2/09	2103	Atmospheric RS	138
12/3/09	2104	Troy Extraction Attempt; MI “BellyRock”	138
12/4/09–12/7/09	2105–2106	Atmospheric RS; APXS Argon	138
12/9/09	2109	Troy Extraction Attempt; MI “BellyRock”	138
12/10/09–12/12/09	2110–2112	Atmospheric RS	138
12/13/09	2113	Troy Extraction Attempt; MI “BellyRock”	138
12/14/09	2114	Pancam 13F “Von Braun,” “Pioneer Mound”	138
12/15/09	2115	Pancam 13F tailings and “Von Braun”; Pancam middle wheels	138
12/16/09	2116	MI “BellyRock”; Pancam 13F “Von Braun”	138
12/17/09	2117	Troy Extraction Attempt; MI “BellyRock”; Pancam 13F “Von Braun”; Pancam middle wheels	138
12/18/09	2118	Troy Extraction Attempt; MI “BellyRock”; Pancam 13F tailings	138
12/19/09	2119	Pancam 13F tailings	138
12/20/09	2120	Troy Extraction Attempt; MI “BellyRock”	138
12/21/09	2121	Atmospheric RS	138
12/22/09	2122	Troy Extraction Attempt; MI “BellyRock”; Pancam 13F tailings	138
12/23/09	2123	Pancam 13F tailings	138
12/24/09	2124	Pancam superres “South Valley”	138
12/25/09	2125	Pancam superres “Pioneer Mound”	138
12/26/09	2126	Troy Extraction Attempt; MI “BellyRock”; Pancam 13F tailings	138
12/27/09	2127	Pancam 13F tailings	138
12/28/09–12/29/09	2128–2129	Runout	138
12/30/09	2130	Troy Extraction Attempt; MI “BellyRock”	138
12/31/09	2131	Pancam 13F Deck	138
1/1/10	2132	Troy Extraction Attempt; MI “BellyRock”	138
1/2/10–1/4/10	2133–2135	Atmospheric RS	138
1/5/10	2136	Troy Extraction Attempt; MI “BellyRock”	138
1/6/10	2137	Atmospheric RS	138
1/7/10	2138	Troy Extraction Attempt; MI “BellyRock”	138
1/8/10	2139	Atmospheric RS	138
1/9/10	2140	Troy Extraction Attempt; MI “BellyRock”	138
1/10/10–1/11/10	2141–2142	Atmospheric RS	138
1/12/10	2143	Troy Extraction Attempt; MI “BellyRock”	138
1/13/10	2144	Atmospheric RS	138
1/14/10	2145	Troy Extraction Attempt; MI “BellyRock”	138
1/15/10	2146	Atmospheric RS	138
1/16/10	2147	Troy Extraction Attempt; MI “BellyRock”	138
1/17/10–1/18/10	2148–2149	Atmospheric RS	138
1/19/10	2150	Troy Extraction Attempt	138
1/20/10	2151	MI “BellyRock”	138
1/21/10	2152–2169	Troy Extraction Attempts, followed by preparations for winter	138

^aRS, remote sensing; IDD, Instrument Deployment Device. Other acronyms defined in Table 1.

2010). The values for the effective dynamic coefficient of friction for the driven wheels (0.3) and the inoperative right front wheel (0.5) were chosen to replicate “sandbox” tests with the engineering test rover at the Jet Propulsion Laboratory.

[6] Five-wheel forward drive simulations on flat surfaces using the parameters described in the last paragraph show that the pushed right front wheel underwent a periodic stick-slip motion and encountered a resisting force of up to 500 N. On the other hand, during backward drives, the value was reduced to 75 N. The difference in values for forward as opposed to rearward driving is associated with increased normal forces and thus soil strength on the right front wheel due to compression of the forward rocker arm during the forward motion of the rover. Considerable yaw was observed during forward drives and only a slight yaw during backward drives. Similar results were obtained for drive simulations on slopes, with the addition of downhill slip magnitude dependent on tilt angle and drive azimuth. Although more complicated models with deformable soils could be employed, the simple frictional model replicates the dynamics of the vehicle well enough on flat and tilted surfaces to

demonstrate that the preferred drive direction for Spirit is backward.

[7] Even though yaw changes were minimized during backward drives, visual odometry was often utilized during five-wheel drive sessions to help keep Spirit on a predefined course, both for fine maneuvering to targets and for long drives in complex terrains [Maimone *et al.*, 2007]. Visual odometry consisted of repeated stereo imaging of nearby targets and using those fixed target positions to update rover motions to stay on course. This worked well, except when climbing soil-covered slopes with tilts more than a few degrees. As discussed in section 5 of this paper, significant wheel slippage, sinkage, and sliding were encountered in this latter case.

3. Winter Campaign on North Slope of Home Plate

[8] Spirit is located at 14.5 degrees south areocentric latitude [Arvidson *et al.*, 2004]. Spirit was exploring the top of Home Plate during its third southern hemisphere fall season on Mars. When the approaching winter made it necessary to



Figure 3. Front Hazcam image acquired while Spirit was in the valley to the north of Home Plate, after a backward drive from the winter campaign site and maneuvering to place the IDD within reach of the nodular, broken rock, Stapledon. APXS data indicate that Stapledon consists of 72% by weight of SiO_2 . Note similar easily broken material in front of and to left side of the right front wheel. Hazcam frame 2F285542810RSLAZAQ1214L0MZ acquired on sol 1793.

tilt the rover toward the north as much as possible the lowest-risk plan was to drive across the relatively flat top of Home Plate and descend onto its northern slope, given the rover's limited ability to climb up slopes (Figure 1). The successful descent on sol 1406 achieved a 13° northerly tilt. Subsequent short downhill drives increased insolation. For example, tilts of 22, 27, and 29 degrees were achieved on sols 1440, 1463, and 1464, respectively. On sol 1763 the first drive away from the winter site was undertaken by driving uphill to get back onto Home Plate (Figure 1). The intent was to drive across the relatively flat top of Home Plate, with extensive bedrock exposures and relatively easy driving conditions, to head south toward von Braun and Goddard (Figure 1). Unfortunately, because of extensive slippage and sliding, Spirit was unable to get back up onto the top of Home Plate. The vehicle was then commanded to drive downhill as an initial step to circumnavigate around Home Plate by traversing the valleys that border it. On sol 1782, the rover drove into the valley to the north of Home Plate.

[9] During its winter stay on the northern slope of Home Plate, Spirit acquired the “Tuskegee” and “Bonestell” Pancam panoramas, monitored the surface and atmosphere, and acquired in situ observations for the rock targets Chanute, Freeman, and Wendell Pruitt. The RAT was used to brush dust coatings from the rock targets. Grinding was precluded because of bit wear (Table 1). The rock measurements resemble observations made at other localities within the upper stratigraphic section on Home Plate and show a dominantly basaltic composition with a contribution from P_2O_5 and TiO_2 -rich rocks of the Wishstone and Watchtower

classes [e.g., Gellert *et al.*, 2006]. In situ observations were also acquired for the soil target Arthur C. Harmon and closely resemble those for typical basaltic soil encountered elsewhere within the Inner Basin.

4. Trip to Troy

[10] After extensive analyses by the science and mobility teams, the route toward von Braun and Goddard was selected to be clockwise in the northern valley to a low-tilt “on ramp” that might allow an ascent onto Home Plate for the drives to the south. MiniTES observations acquired from the winter campaign site of low nodular outcrops in the northern valley indicated the presence of silica-rich materials (S. Ruff *et al.*, Characteristics, distribution, and significance of opaline silica in Gusev crater, manuscript in preparation, 2010). Thus, one of the first in situ targets after leaving the winter site was Stapledon, a group of nodular outcrops that the rover first drove over to expose relatively fresh materials (Figure 3). APXS measurements showed a SiO_2 content of 72%, confirming the presence of silica-rich materials in the northern valley, in addition to the eastern valley surrounding Home Plate (Figure 1) [Squyres *et al.*, 2008; S. Ruff *et al.*, manuscript in preparation, 2010].

[11] Mobility was found to be very difficult while attempting to climb over soil-covered, northeast-trending ridges in the valley on the northeastern side of Home Plate (Figure 1). Spirit experienced significant wheel sinkage and high slip as well as lateral and longitudinal sliding. One



Figure 4. Pancam false color image of disturbed area C. L. Moore where whitish material was exposed by dragging the right front wheel during backward drive maneuvers on sol 1813 to try and climb onto Home Plate. Note red nature of the undisturbed surface in between patches of dark sand. Pancam frames 2P287401133RSDAZJAP2544L2MZ (0.753 μm center wavelength as red), 2P287401156RSLAZJAP2544L5MZ (0.535 μm as green), and 2P287401169RSLAZJAP2544L7MZ (0.432 μm as blue), acquired on sol 1814.

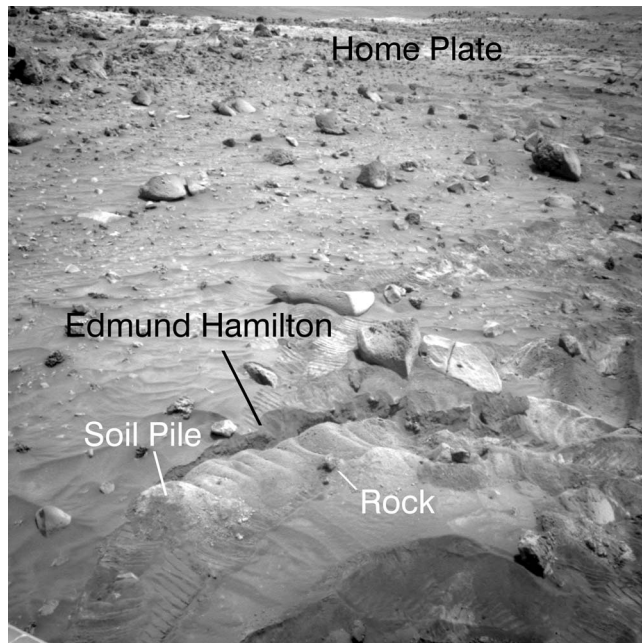


Figure 5. Navcam image of Edmund Hamilton disturbed soil area generated when Spirit was driving and attempted turns in place on sols 1836–1837. The left wheels excavated bright materials as a set of “sand waves.” Navcam frame 2N2899977045RSDBOEP0675L0MZ acquired on sol 1843.

illustrative example is C. L. Moore, an area where subsurface soil was excavated largely by the right front wheel on sols 1811 and 1813 (Figure 4). While driving backward on sol 1811, Spirit autonomously executed several forward and backward arc turns to correct its heading. These motions exhumed the left side of C. L. Moore and exposed bright soil excavated from just beneath the surface. On sol 1813 Spirit executed another set of arc turns to rotate to the correct course heading before driving backward. These motions further excavated bright soils and produced the linear segment shown near the lower right corner of Figure 4. The right front wheel was dragged across the surface during the arc turns with shear stress sufficient to cause soil failure and excavation of underlying materials. The undisturbed soil adjacent to C. L. Moore exposed between patches of relatively dark windblown sand displays a red hue that was not observed previously in soils located in the plains surrounding the Columbia Hills, or even within most areas within the Hills proper (Figure 4). Unfortunately, because of time constraints, in situ measurements were not made for the C. L. Moore target.

[12] A second example of significant soil excavation on the northeastern corner of Home Plate is the Edmund Hamilton area (Figures 5–6). When Spirit autonomously executed an extensive set of turns in place on sols 1836 and 1837, the left wheels produced a set of regularly spaced soil mounds as slippage disturbed the soil and the wheels sank. In this case the wheels created regularly spaced soil mounds when they slipped extensively on loose or weakly consolidated soils. The wheel cleats transported soil to the rear of the slipping wheels and formed mounds with flanks at the angle of repose of the soil. As the size of a mound increased, the

wheel gained additional thrust through shear along the wheel-mound interface, allowing centimeter-scale forward motion. As the rover moved in the drive direction, the soil mound experienced slope failure, forming a peak and also decreasing the available wheel thrust due to reduction in the length of the wheel-soil interface. Wheel forward motion slowed and the mound formation process began again, forming periodic “waves” of soil.

[13] In the two examples cited above, Spirit experienced extensive slippage and increased resistance due to partial wheel burials. This resistance can be modeled using classic Bekker-Wong terramechanics theory [Bekker, 1969; Wong, 2003]. Two characteristic resistances are important. First the contact between the wheel surface and soil provides a compaction resistance to motion in the drive direction for a driven wheel. This resistance increases as the extent of wheel burial increases. Second, wheels that are driven, pushed, or towed bulldoze soil in the drive direction, generating additional resistance. The summed resistances were not sufficient to immobilize the vehicle at either C. L. Moore or Edmund Hamilton. Unfortunately, in situ measurements were not made for either the C. L. Moore or Edmund Hamilton areas due to time constraints associated with the need to get to von Braun and Goddard. The colors of the soils excavated at both sites resemble those of the excavated sulfate-rich soils at Tyrone and Arad [e.g., Wang *et al.*, 2008; Rice *et al.*, 2010], indicating that similar materials might have been exposed by wheel motions.

[14] Multiple attempts were made to drive Spirit clockwise around the northeastern side of Home Plate. Extensive

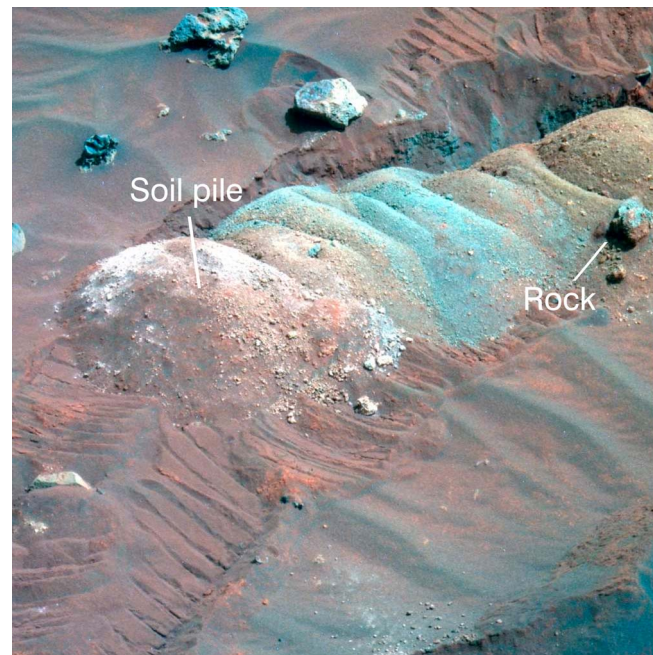


Figure 6. Pancam false color image of Edmund Hamilton disturbed area. The “sand waves” are associated with left wheel motions as described in the text. Note weak layering in far wall of trench dug by the left wheels. Pancam frames 2P290424417RSLBOFP2555L2MZ, 2P290424450RSLBOF4P2555L5MZ, and 2P290424478RSLBOF4P2555L7MZ acquired on sol 1848.



Figure 7. Front Hazcam view showing relatively bright disturbed soils excavated by dragging the right front wheel backward. John Wesley Powell is the target for which the MI data are shown in the lower left. APXS data show 28% SO_3 by weight for this target. Hazcam frame 2F291581504RSLB0OAP1214L0MZ acquired on sol 1861.

sinkage, slippage, and yaw about the right front wheel, combined with downhill slip, precluded climbing over the northeasterly trending ridges extending from this side of Home Plate. After extensive discussion between the science and engineering teams, Spirit began to circumnavigate counterclockwise around Home Plate through the northern

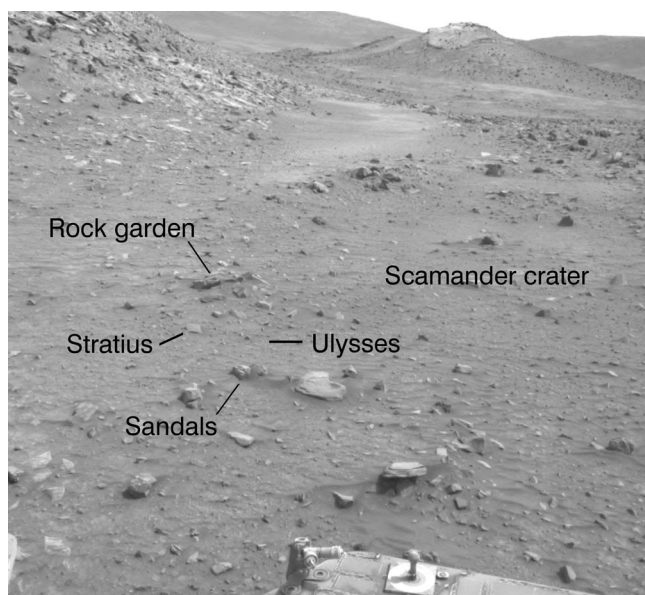


Figure 8. Sol 1870 Navcam image looking to the south with some of the same features shown as labeled on the Hazcam images shown in Figures 9–10 and the topographic map in Figure 11. Frame 2N292380548RSDB159P0691L0MZ.

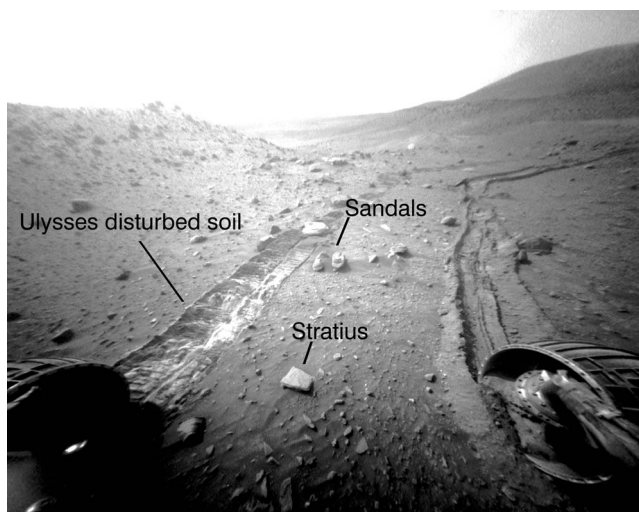


Figure 9. Sol 1871 Front Hazcam image showing relatively bright soils disturbed by left front wheel, along with features also observed in the sol 1870 approach mosaic. Spirit was driving backward. Frame 2F292473825RSLB188P1212L0MZ.

valley and then south through the western valley (Figure 1). The western valley had been imaged in detail when Spirit was on the western side of Home Plate, but there was still concern that the soil and substrate characteristics for this valley were uncertain.

[15] Drives from the northeastern side of Home Plate to the west and then south into western valley were uneventful, with the exception of exposing a long section of relatively bright soil (exposed by dragging the right front wheel during a backward drive) just after entering the western valley (Figure 7). In situ observations on sol 1861 show that this material (target John Wesley Powell, Figures 1 and 7) is composed of sulfate-rich (28% SO_3), fine-grained sands mixed with basaltic materials. Mobility was nominal during the drives through sol 1870 (Figure 1).

5. Embedding at Troy

[16] Drives beginning on sol 1871 through 1899 caused Spirit to become embedded in the sands of Troy. The 1870 drive placed Spirit ~9 m to the northwest of an area subsequently named Troy (Figure 8). The backward drive to Troy on sol 1871 was intended to drive up a modest slope and onto a plateau (informally named the sidewalk, Figure 1) that extended from the southwestern side of Home Plate (Figure 8). The drive indeed positioned Spirit on the slope, but with an unexpected yaw. The Front Hazcam images from sol 1871 showed that the left wheels uncovered bright soil and sank more deeply than they had previously in the western valley (Figure 9). Subsequent attempts were made to drive onto the sidewalk and continue south. After Spirit's wheels became embedded further and the left middle wheel drive actuator stalled on sol 1899 the MER project declared a moratorium on further drives. Drives began again on sol 2078 after an extensive set of sand box experiments and analyses focused on the optimum drive procedures for extrication. For reference, on sol 2072 the vehicle's yaw was estimated from its accelerometers to be 340° clockwise from



Figure 10. Front Hazcam view taken on sol 2072, before extrication activities began, but after Spirit stopped driving on sol 1899. Key targets are labeled. Ulysses is the excavated area in front of the left front wheel. The press test target represents use of the RAT as a bevameter to push into the soil to determine static sinkage as a function of applied normal stress. The Ulysses trench in front of the left front wheel is approximately 42 cm wide and 8 cm deep at its deepest point, relative to the undisturbed surface to the east. Frame 2F310307243RALB200P1214L0M1.

north, the pitch was 1° toward the northwest, and the roll was 12° toward the southwest. Spirit at that point in time was tilted 4° to the south.

[17] During the final drives prior to the drive stand down, the active wheels experienced almost 100% slippage and became substantially buried. In addition, the wheel cleats became coated with fine-grained materials, lowering the effective coefficient of friction between the wheels and soils. The drives exposed bright soils around the left front wheel in an area named Ulysses (Figure 10). During the final backward drives, the left front wheel generated a set of soil “waves.” As noted earlier, wheels that experience high slippage and that sink into loose or weakly cohesive soils typically form these “waves.” Navcam images and localization data from sol 1870 indicate that Spirit had become embedded with its left wheels within and right wheels outside of the wall and rim of a highly degraded crater, subsequently named Scamander (Figure 11). Scamander crater is approximately 8 m wide and 25 cm deep. The “Rock Garden” located under Spirit is one of several groups of rocks on the crater rim.

[18] Two numerical simulations of Spirit’s embedding at Troy provide insight into the available thrust from the drive wheels and the resistance due to soils and any buried rocks surrounding the wheels. For the first simulation it was assumed that Coulomb frictional parameters limit the thrust available from the five drive wheels, as discussed in section 2 of this paper. The static coefficient of friction was taken from the steepest slope (32 degrees) observed in the

Ulysses disturbed soils, with cohesion assumed to be minimal. Static wheel sinkage was modeled by placing the two hundred element software model of the rover [Lindemann and Voorhees, 2005] onto a digital elevation map generated from sol 1870 Navcam approach images and letting its wheels settle into the subsurface according to a power law relationship between normal force and sinkage. The resistance due to soil around the wheels could not be explicitly modeled using this approach. Rather, a simulated spring representing this resisting force was attached to the rover body and fixed to a static position. Drives were run in both forward and backward directions. To simulate the nearly 100% wheel slip, the resisting force needed to be 30% higher than the thrust available for the five driving wheels.

[19] The second method for calculating the resisting forces used the Bekker-Wong theory, given estimates of the degree of burial for each wheel that were derived from Navcam and Hazcam image data, together with rover yaw, pitch, roll from accelerometer data, and rocker and bogie suspension angle values. Values for the Bekker-Wong parameters were derived from a combination of information from soil simulants used for MER single wheel tests [Richter et al., 2006] and internal friction angle parameters from Ulysses data. Again, the soil resistance derived from this modeling exceeded the available drive thrust by a significant amount. Within error the two analyses agree and

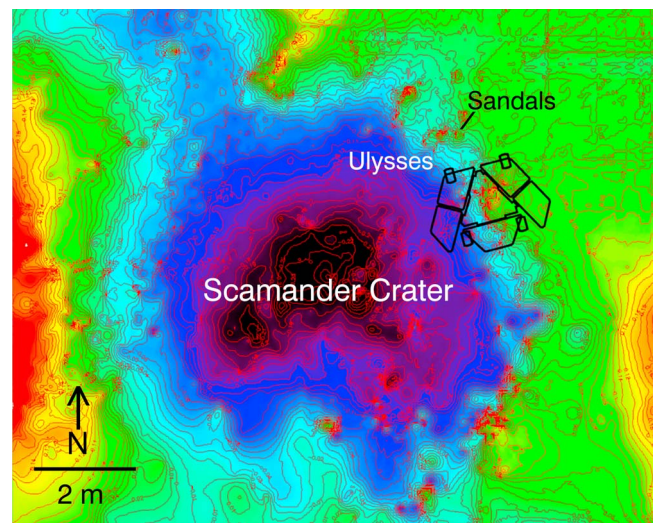


Figure 11. Topographic map for Scamander crater, approximately 8 m wide and 0.25 m deep, generated from the sol 1870 drive direction Navcam image mosaic. Regional planar tilt to the northwest was removed to emphasize local topographic variations. Relief is approximately 3 m with red colors assigned to highest regions and black to lowest regions. Sandals are a pair of rocks shown in Figures 8–10. The features beneath the rover represent rocks within the Rock garden, again as shown in Figure 8. The “sidewalk” is the relatively flat area to the southeast of Spirit and the destination for the post sol 1870 drives. During its last 10 extrication drives Spirit moved 34 cm backward and to the southeast, placing the left wheels further into Scamander crater.

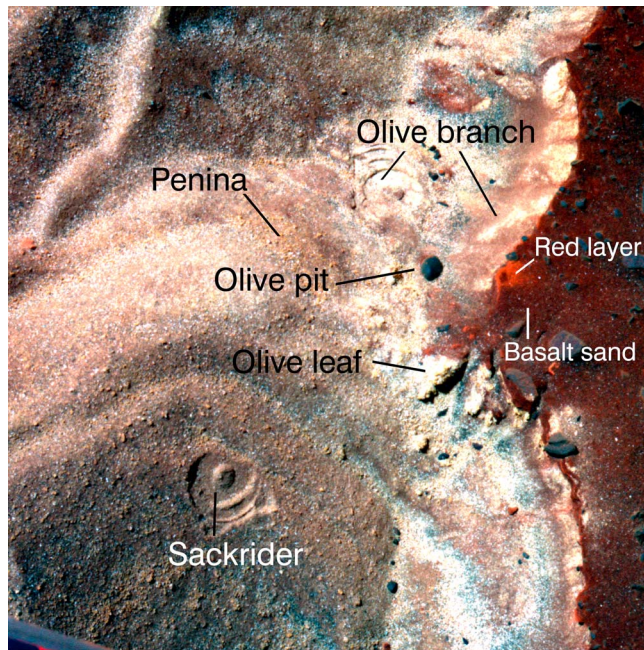


Figure 12. Sol 1933 Pancam false color image showing various IDD targets in Ulysses. The data were acquired during the middle of the extensive IDD campaign in this area. MB faceplate imprints are evident for target Sackrider, and several imprints are evident with lateral displacements for Olive Branch targets. Penina data were not yet acquired. Olive leaf is a set of targets on bright crust exposed on the eastern wall of Ulysses and just beneath the undisturbed surface. The red layer occurs in a number of places and exists at the surface where not covered by dark basaltic sands or rocks. Pancam frames 2P297975975SRSLB1ESP2382L2M2, 2P297976112SRSLB1ESP2382L5M2, 2P297976177SRSLB1ESP2382L7M2.

help to explain why Spirit became immobilized as its wheels dug into the soil at high slip rates.

6. Troy Soil Measurement Campaign

[20] During the period when driving was prohibited, an extensive measurement campaign was implemented to characterize the materials exposed within the Instrument Deployment Device (IDD) work volume and the surrounding areas (Figures 10 and 12). Multiple targets in Ulysses were selected to investigate the range of materials evident in the Pancam color images (e.g., Figure 12). The targets group into three categories. The first was within the soil “waves” in Ulysses that the left front wheel excavated during its backward drives before the sol 1899 drive stand down. Sackrider, an area that appeared brown to gray in Pancam false color images (e.g., Figure 12), was the first of these sites for acquisition of Microscopic Imager (MI), Alpha Particle X-Ray Spectrometer (APXS), and Mössbauer Spectrometer (MB) data (Table 1), with MB faceplate imprints used to help confirm the surface location. Three sites were examined within Penina, an exhumed area of soil with a yellow-brown color. Each of three Penina targets was

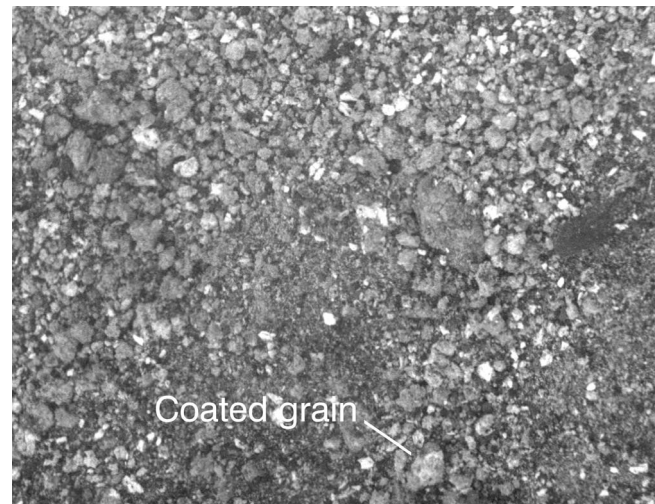


Figure 13. Portion of an MI image of the Penina 3 target acquired on sol 1986 when the target was shadowed. Image covers ~ 1.5 cm across and shows angular, sand-sized grains. Label points to one of several grains that are interpreted to be coated with a bright material. MI frame 2M302672578FFLB1E5P2956M2M1.

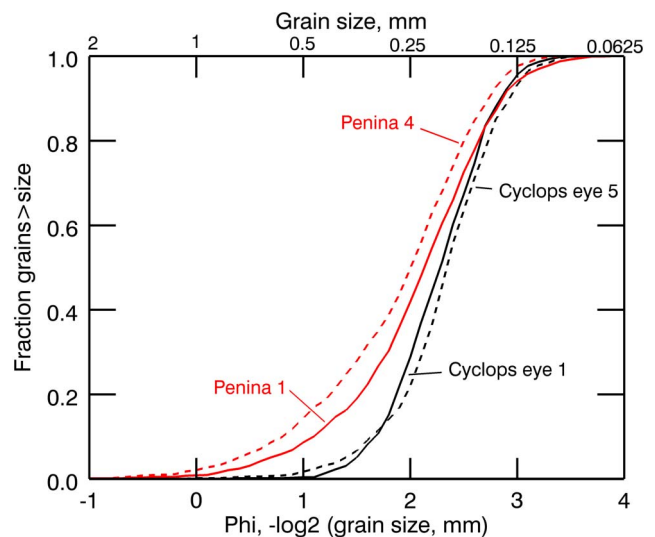


Figure 14. Grain size analyses presented as cumulative percent of grains larger than some size as a function of grain mean diameter in Φ units, which are $-\log_2(\text{diameter in mm})$. Graphic means, standard deviations, and skewness (skew toward coarse or fine sizes relative to log normal distribution) computed using formulae of *Lewis and McConchie* [1994] and presented in Table 3. The curves were derived from counts using MI data, computing mean grain diameters as the average of long and short dimensions. Penina targets are skewed toward larger grains relative to the Cyclops data. The later Penina 4 target is skewed even more toward larger grains than the earlier target, Penina 1. Further, the Cyclops targets are well sorted as compared to the other targets.

Table 3. Troy Target Grain Size Statistics^a

Parameter	Olive Branch 1	Sackrider	Penina 1	Penina 4	Cyclops Eye 1	Cyclops Eye 5
Mean	1.99	2.18	2.08	1.89	2.27	2.33
Graphic standard deviation, σ	0.60	0.67	0.70	0.75	0.45	0.48
Skewness	-0.11	-0.13	-0.16	-0.27	-0.04	-0.09

^aUnits are Φ . Note that these are based on number of grains smaller than some fraction and not weight percentages, which is the typical method used for reporting grain size analyses for terrestrial soils and sediments.

displaced laterally from the others in order to provide compositional mixing trends for APXS analyses. A fourth Penina target was also investigated 83 sols after the other Penina targets in order to search for textural and compositional changes that might be caused by, for example, wind erosion of the particles. Finally, the RAT was used as a bevameter to press into the soil in Ulysses using a pre-defined load to evaluate sinkage as a function of applied normal stress.

[21] The second category of targets included MIs on Olive tree and multiple Olive branch and Olive leaf targets for which MI, APXS, and MB data were acquired. These targets focused on the relatively bright material coming from the top of the eastern “cliff” bordering Ulysses and deposited on the “valley” wall (Figure 12). The third target category included undisturbed soil surfaces in order to test the hypothesis that the brown, yellow, and white material in Ulysses exist beneath the surface to the east of Ulysses. The first, Cyclops eye, was located ~10 cm to the east of the Ulysses eastern wall where three laterally displaced sets of MI and APXS measurements (Cyclops eye 1–3) were acquired, along with one MB measurement (Figure 10). The Cyclops eye 3 target was also brushed after a grind scan, and MI, APXS, and MB data were acquired (Cyclops eye 4). Finally, another grind scan was implemented followed by another suite of measurements (Cyclops eye 5). The grind scan was to be followed by an actual grind using the metal grind pads as substitutes for the grind bits (Table 1). This action failed, although the grind scan did expose relatively bright material for measurements. An additional target was selected 10 cm to the east of Cyclops eye. This target, Polyphemus eye (Figure 10), was ground twice with measurements after each RAT activity (Polyphemus eye 1–2). A final undisturbed soil MI, APXS, and MB measurement set was conducted on the target, Thoosa, located near the Polyphemus eye targets.

[22] MI observations show that Sackrider and Penina consist of angular, poorly sorted, sand-sized particles (Figures 13–14 and Table 3) [Siebach, 2010]. Penina 4 exhibits the coarsest grains, interpreted to be due to winnowing of fine grains by winds during the period between acquisition of Penina 3 and 4 MI observations. Further, the particles are bimodal in brightness, with several examples in which relatively bright material can be seen coating dark grains. Also seen are dark grains without coatings and grains composed of bright material. The Olive tree target shows that the top of the Ulysses eastern cliff consists of a series of ~1 cm crust-like layers of cemented grains that provide relatively bright material as scree down the sides of the Ulysses trench (Figures 10 and 15). The Olive leaf targets, again a crusty layer at the top of the Ulysses eastern cliff, show similar textures as the Olive tree target. The crusts for both targets are dominated by poorly sorted sands with sizes

similar to those found for Ulysses sands. Below the more competent layer the surface slopes less steeply, consistent with exposures of less indurated materials.

[23] As noted, the Cyclops, Polyphemus eye, and Thoosa targets were located to the east of the Ulysses cliff and wall (Figures 10 and 16). The MI data for the undisturbed surfaces show a particle size distribution that is skewed toward finer sizes and indicates better sorting than the material within Ulysses (Figure 14 and Table 3). A subpopulation of dark, well-rounded grains of likely aeolian origin is also evident for these undisturbed targets. The RAT brushing and grinding in Cyclops eye, based on Pancam stereo data, excavated ~0.5 cm beneath the surface by brushing and exhumed an additional ~0.5 cm by using the RAT grind scan capability. The final excavation exposed white, sand-sized grains (Figures 16–17). These materials look similar to the bright material on the cliff and slopes within Ulysses, including brighter material coating darker grains. Pancam and MI coverage of the Thoosa and both Polyphemus eye targets (as deep as ~1 cm), on the other hand, look rather similar to the undisturbed Cyclops eye targets.

[24] Mineralogical information derived from Pancam 13 filter spectral observations and MB observations of iron mineralogy and oxidation state, together with elemental abundances inferred from APXS data, provide important additional information about materials encountered during the in situ measurement campaign. The approach taken in this paper is to first use the MB data to constrain iron

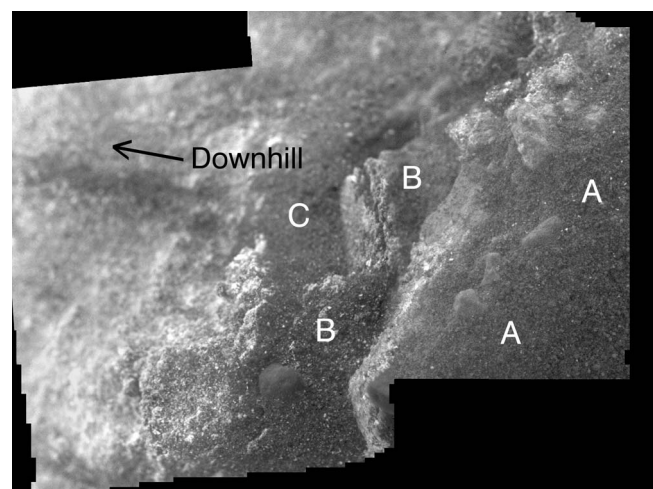


Figure 15. MI mosaic of Olive tree, a soil crust underlying the cliff on the eastern side of the Ulysses disturbed soil zone. See Figure 10 for location. The letters A, B, and C are located on plateaus associated with discrete crust layers exposed during Spirit’s embedding. Data acquired on sol 1927 and processed as a merged focal section.

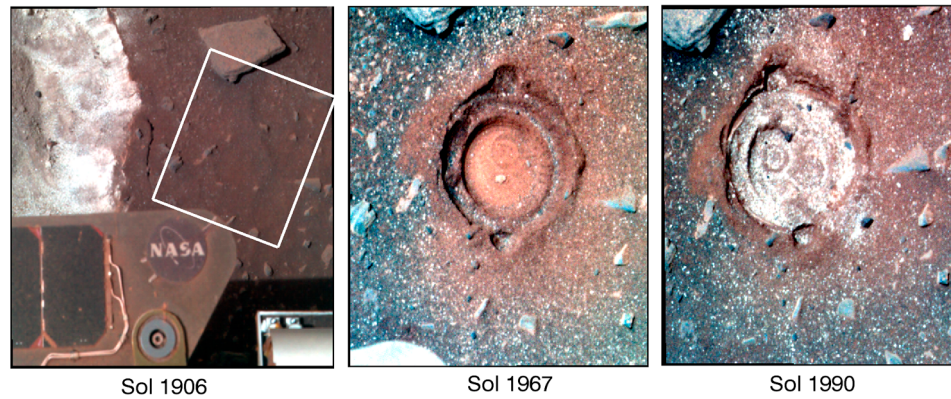


Figure 16. Pancam false color views of the sequential boring into Cyclops eye using the RAT. The location is shown in Figure 10, and the experiment was meant to search for the lateral extent of bright soils to the east of Ulysses. (left) Frame was acquired on sol 1906, before any RAT activities, and shows the approximate location of IDD measurements that define Cyclops eye 1 to 3, with offsets to provide compositional trends. (middle) The sol 1967 data were acquired after a RAT brush exposed a red layer (Cyclops eye 4) similar to the layer observed on the undisturbed surface at the edge of Ulysses (see Figure 12). (right) Image was acquired after a RAT grind scan removed the red layer and exposed white granular material (Cyclops eye 5). RAT holes are approximately 4 cm in width.

mineralogy and oxidation state and then to use these results to help interpret Pancam spectral data. This is a valid approach because the dominant features in Pancam data (0.4 to $1.0 \mu\text{m}$) result from the presence of iron bearing minerals [Bell *et al.*, 2003]. A ferric-bearing sulfate phase, with a similar MB signature as found for the Arad sulfate-rich soils excavated by Spirit in the northern part of the Inner Basin (R. V. Morris *et al.*, manuscript in preparation, 2010), dominates the iron mineralogy for the Ulysses targets, particularly for the Olive leaf target (Table 4). The values of the quadruple splitting are not consistent with ferricopiapite as suggest by Lane *et al.* [2008] for Paso Robles and by Johnson *et al.* [2007] for Home Plate sulfate-rich soils. The reason is that the two ferric doublets, as reported for ferricopiapite [Lane *et al.*, 2008], are not detected for the Mars data (R. V. Morris *et al.*, manuscript in preparation, 2010). By analogy with Arad, these sulfate-rich soils are hydrated on the basis of excess light elements, perhaps with nine waters of hydration as compared to the twenty needed for ferricopiate [Campbell *et al.*, 2008]. Detailed analyses of the likely phases are reported by Morris *et al.* (manuscript in preparation, 2010).

[25] Correspondence analysis was applied to MB data set shown in Table 4 to better understand dominant trends [e.g., Larsen *et al.*, 2000; Arvidson *et al.*, 2006, 2008]. Ninety-six percent of the variance can be explained by the first two factors, with 90% loaded onto the first factor (Figure 18). Factor loadings define two groups of targets, with the Cyclops eye 3, 4 and Polyphemus eye targets dominated by olivine and pyroxene, with the addition of nanophase iron oxide for the surface or near-surface targets. As noted, Ulysses targets are dominated by a ferric sulfate phase. They also show an affinity for hematite. The Cyclops eye 5 target is located at the intersections of linear projections from the Ulysses materials and the surface materials. Increasing iron oxidation state trends follow the nanophase iron oxide abundance trends for surface targets and increasing amounts of hematite and ferric sulfate for the subsurface targets. These results are consistent with the dominance of basaltic

materials and nanophase iron oxide dust or coatings at the surface, with increased hematite and ferric sulfate abundances just beneath the surface to the west of the Polyphemus eye targets.

[26] Pancam 13 filter data acquired on sol 1933 (Figure 12) were coregistered and calibrated to reflectance using the Pancam calibration target following procedures defined by Bell *et al.* [2003, 2006]. The seven left eye images (0.432 to $0.753 \mu\text{m}$) were then run through a noise-weighted principal components analysis and the first two components, accounting for 98% of the variance of the data, were used to

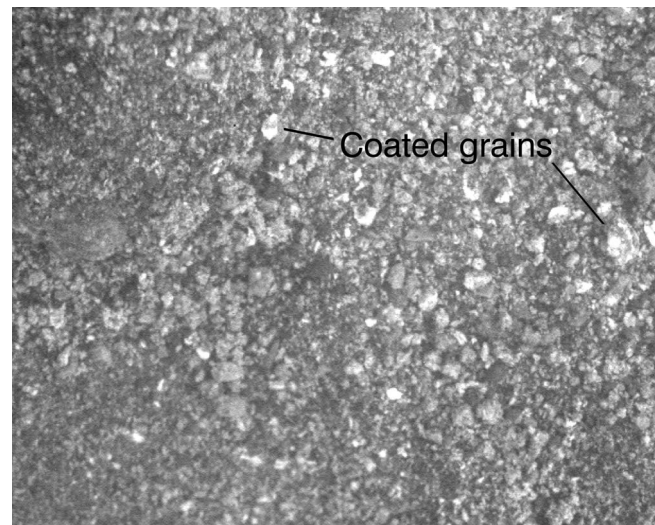


Figure 17. Portion of an MI image of the bottom left surface of Cyclops eye 5 acquired on sol 1990 when the target was in shadow. Frame covers ~ 1.5 cm in width and mean grain size is 2.03Φ (see Table 4). Label points to two grains that are interpreted to be coated with a bright material. MI frame 2M303036777EFFB1E5P2936M2F1.

Table 4. MB Iron Mineralogy^a

Sol, Type, and Name	Ol	Px	Fe ⁺³ Sulfate	Hm	NanoFeOxide	Fe ⁺³ /Fe _T
A1923SD Sackrider	25	10	58	7	0	0.65
A1930SD Olive branch 2	25	16	50	9	0	0.58
A1937SD Penina 1 (combined A1937 and A1943)	16	14	66	4	0	0.70
A1949SU Cyclops eye 3	43	37	0	3	17	0.19
A1970SR Cyclops eye 4	29	46	5	2	18	0.23
A1983SR Cyclops eye 5	28	36	21	6	9	0.35
A1997SR Polyphemus eye 2	23	44	0	8	26	0.30
A2010RD Olive leaf 1	6	8	79	7	0	0.85
A2026SD Penina 4	23	17	60	8	0	0.60
A2053SU Thoosa	34	35	0	8	23	0.31

^aA refers to MER A or Spirit. The sol is next, followed by SD for disturbed soil, SU for undisturbed soil, SR for ratted soil, RD for disturbed rock (actually soil crust). From Morris et al. (manuscript in preparation, 2010).

retrieve spectral end-members (Figure 19). Olive pit, a dark pebble on the floor of Ulysses, plots as an end-member along a mixing line, with red exposures on the undisturbed surface to the east of Ulysses as the other end-member. Dark sandy patches on the undisturbed surface, interpreted to be basaltic sands, fall on the mixing line. Spectra for Sackrider, Penina, and Olive leaf targets deviate from the mixing line and form a diffuse mixing zone with Olive leaf as an end-member.

[27] Pancam spectra for the targets labeled in Figures 12 and 19 are shown in Figure 20. All of the Pancam data

exhibit a ferric edge shortward of 0.7 μm that appears in almost all spectra of Mars and indicates the presence of at least minor amounts of nanophase iron oxide for all targets. The dark patches on the undisturbed surface are consistent with the dominance of olivine and pyroxene based on shallow Fe⁺² electronic absorptions at the longest wavelengths. Spectra for Olive pit (not shown) are consistent with a largely unweathered basaltic mineralogy. The red layer on the undisturbed surface is characterized by a very strong ferric edge, consistent with a spectral dominance of nanophase iron oxide.

[28] Olive leaf and Penina spectra show a subtle absorption feature between 0.75 and 0.9 μm . The Sackrider spectrum shows the subtle downturn at 0.75 μm evident in Olive leaf and Penina spectra, but not the upturn at longer wavelengths.

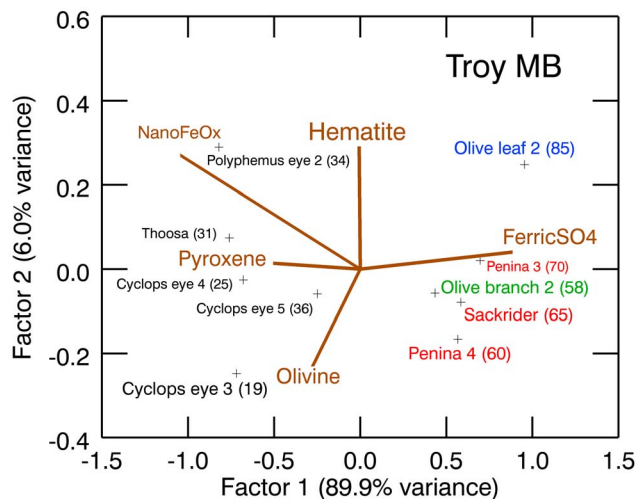


Figure 18. MB based results for the proportions of iron bearing phases for Troy soil measurements (see Table 4) were used to solve for and plot factor loadings using correspondence analysis. The first two factors control 96% of the variance of the data set. Numbers in parentheses represent Fe⁺³/Fe_{total} in percent. Cyclops eye 3 is an undisturbed surface, Cyclops eye 4 is the brushed surface exposing red material, and Cyclops eye 5 is the surface exposing white material (see Figure 16). Polyphemus eye 2 is the deepest hole for that RAT grinding experiment. Olive leaf and Olive branch targets were on relatively bright material on the cliff and scree slope of Ulysses whereas Penina and Sackrider were in the interior of the Ulysses disturbed soil area. These ferric sulfate-rich materials also show an affinity for hematite.

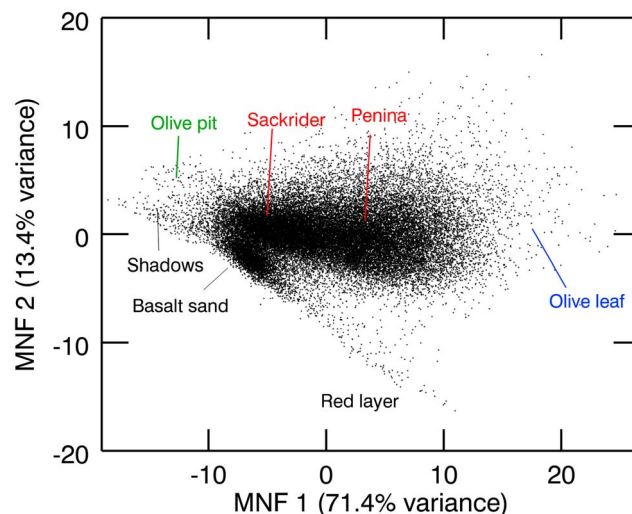


Figure 19. Plot of the first two principal components (expressed as minimum noise fractions or MNFs) for the sol 1933 Pancam 6 filter left eye wavelengths (0.432 to 0.753 μm). The left eye data were chosen because they have more variance than the right eye data and because geometric warping of the right eye to the left eye produced data gaps that lowered the number of pixels available for principal components analysis. The first two factors control 85% of the six-dimensional spectral data set variance. Mixing patterns are discussed in the text.

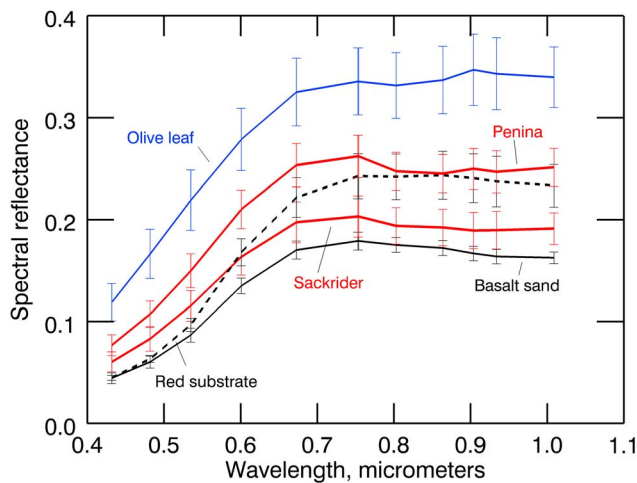


Figure 20. Pancam spectra retrieved for targets in the sol 1933 Pancam data shown in Figure 12. The spectral region shown is dominated by electronic transition absorption features associated with iron, including the ubiquitous ferric edge at short wavelengths and ferrous bands associated with iron-bearing olivine and pyroxene at long wavelengths. Note that the red layer (location shown in Figure 12) has a particularly strong ferric edge. Olive leaf shows a bright spectral reflectance and a subtle absorption from 0.75 to 0.9 μm that is consistent with the presence of ferric sulfates with modest water content, as discussed in the text. This signature is also evident in the spectra for Penina and Sackrider, particularly for continuum removed spectra. Not corrected for cosine of solar incidence angle.

Continuum removed versions of the Olive leaf, Penina, and Sackrider spectra indicate the presence of the subtle feature between 0.75 and 0.9 μm in spectra for all three targets. As noted, the Penina and Sackrider spectra shown in Figure 20

are not end-members, but lie between the Olive leaf position and a relatively diffuse mixing zone defined by Olive pit and red layer end-members. The positions of Sackrider and Penina within the mixing space are probably governed by local tilts, in addition to the amount of ferric sulfate material. In particular, the Sackrider target was tilted away from the sun relative to the Penina target and thus reflecting less radiance toward Pancam when the data were acquired. The subtle absorption feature between 0.75 and 0.9 μm is consistent with spectra obtained experimentally by *Ling et al.* [2009] for moderately hydrated ferric sulfates, e.g., ferric hexahydrate. Thus, the combination of MB, APXS, and Pancam data, using Arad results to help bootstrap inferences, provide a self-consistent conclusion that Ulysses exposes moderately hydrated ferric sulfates.

[29] APXS compositional information for relevant samples from Troy is provided in Table 5. This extensive data set (21 samples and 11 variables) was subject to correspondence analysis to search for trends between samples and oxide compositions. Results are shown in Figure 21 and exhibit trends that are similar to those observed for the MI, MB, and Pancam results. That is, the first factor controls most of the data set variance and is represented by ferric sulfate-rich samples on the right side and basaltic materials on the left side. For example, the shallow Cyclops eye target, along with Thoosa and Polyphemus eye targets, plot on the basaltic side, whereas the Penina and Sackrider targets plot on the ferric sulfate side. In fact, the Penina 3 target, located furthest along the ferric sulfate vector direction, has the highest concentration of SO_3 (36%) of any of the APXS targets for either Spirit or Opportunity. Cyclops eye 5 plots between the two sets of end-members. This mixing line controls 97% of the variance of the data set. The second factor shows that the subsurface targets within the Ulysses area in Scamander crater are rich in ferric sulfate. In addition, the shallow targets, Olive leaf and Olive branch, show affinities for CaO and SiO_2 . This suggests the presence of modest amounts of calcium sulfate and silica, although

Table 5. APXS Compositions as Oxide Weight Percents^a

Sol, Type, and Name	Na_2O	MgO	Al_2O_3	SiO_2	P_2O_5	SO_3	Cl	K_2O	CaO	TiO_2	Cr_2O_3	MnO	FeO
A1925SD Sackrider	1.38	4.46	4.92	28.4	0.79	33.03	0.30	0.14	5.75	0.43	0.43	0.20	19.7
A1927SD Olive branch 1	1.23	3.92	4.74	33.7	0.66	30.91	0.29	0.15	6.60	0.44	0.47	0.16	16.7
A1928SD Olive branch 2	1.38	4.35	5.27	35.0	0.68	28.64	0.31	0.17	5.85	0.48	0.47	0.19	17.1
A1934SD Olive branch 3	1.37	4.39	5.31	36.2	0.70	27.88	0.32	0.19	5.66	0.50	0.45	0.17	16.7
A1935SD Olive branch 4	1.45	4.52	5.71	36.7	0.70	26.66	0.33	0.21	5.48	0.51	0.44	0.19	17.1
A1939SD Penina1	1.08	4.07	4.79	28.7	0.73	34.74	0.29	0.15	5.64	0.37	0.50	0.15	18.7
A1940SD Penina2	0.96	3.91	4.61	28.6	0.76	35.56	0.28	0.12	5.28	0.36	0.51	0.15	18.9
A1941SD Penina3	1.02	3.80	4.50	28.2	0.76	35.82	0.27	0.12	5.42	0.41	0.49	0.15	18.9
A1945SU Cyclops eye 1	2.88	8.82	10.24	45.4	0.78	7.26	0.48	0.37	6.23	0.73	0.34	0.32	16.0
A1946SU Cyclops eye 2	2.83	8.89	10.37	46.0	0.78	6.76	0.46	0.35	6.26	0.72	0.33	0.31	15.9
A1947SU Cyclops eye 3	2.94	9.16	10.38	45.9	0.77	6.20	0.45	0.37	6.25	0.72	0.33	0.30	16.1
A1966SB Cyclops eye 4	2.80	8.16	9.16	45.7	0.87	8.78	0.59	0.36	5.75	0.89	0.37	0.31	16.2
A1967SD Olive branch 5	0.88	5.05	5.37	37.3	0.71	26.76	0.29	0.18	6.40	0.44	0.66	0.18	15.7
A1973SR Cyclops eye 5	2.31	6.85	8.15	40.4	0.80	15.93	0.42	0.32	5.70	0.83	0.46	0.29	17.4
A1979SD Olive pit	1.33	7.51	4.92	36.5	0.63	23.30	0.33	0.12	5.36	0.37	0.51	0.25	18.7
A1981SRPolyphemuseye2	2.65	8.45	9.01	42.9	0.87	9.36	0.65	0.36	6.03	1.02	0.44	0.36	17.7
A1995SRPolyphemuseye3	2.46	8.04	8.88	42.8	0.90	9.80	0.68	0.40	5.97	0.96	0.46	0.36	18.2
A2006RD Olive leaf 1	0.58	3.60	4.03	29.2	0.65	34.20	0.32	0.11	8.35	0.35	0.53	0.15	17.8
A2016RD Olive leaf 2	1.10	4.69	5.25	32.4	0.72	29.30	0.37	0.19	7.66	0.45	0.51	0.16	17.2
A2024SD Penina 4	1.46	5.37	6.16	33.9	0.78	27.94	0.33	0.18	5.63	0.50	0.54	0.18	17.0
A2071SUThoosa	2.87	8.77	9.61	46.1	0.85	6.21	0.62	0.39	6.11	0.80	0.37	0.31	16.9

^a Cr_2O_3 and TiO_2 were not used in correspondence analysis because estimated measurement errors are comparable to retrieved abundances. Same nomenclature as used for MB table. From Morris et al. (manuscript in preparation, 2010).

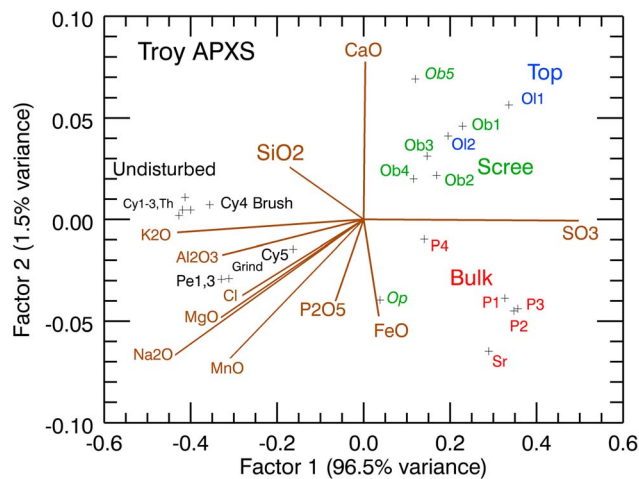


Figure 21. APXS-based correspondence analysis as applied to soils measured while Spirit was embedded at Troy. Oxide compositions are given in Table 5. Factor one dominates the data set variance and represents a mixture between basaltic and sulfate-rich end-members. Factor two allows subtle variations in composition to be inferred, including the CaO and SiO₂-rich Olive leaf and Olive branch materials. Note also the displacement of Cyclops eye 5 away from surface soils toward sulfate-bearing materials here and in Figure 18. Olive branch 5 and Olive pit (shown in italics) represent measurements with significant contamination by dark pebbles of likely basaltic composition. Target names are abbreviated on plot as follows: Ob, Olive branch; P, Penina; Sr, Sackrider; Op, Olive pit; Ol, Olive leaf; Cy, Cyclops eye; Pe, Polyphemus eye; Th, Thoosa.

direct phase detection is not possible with the rover science payload.

7. Troy Extrication Attempts

[30] It is not surprising that Spirit made little progress during the initial extrication attempts that began on sol 2078 (see Table 2 for temporal summary). Motion resistance far exceeded the available thrust and the wheels basically spun in place. In addition, on sol 2104 the right rear wheel drive actuator failed, forcing four wheel drives with only the middle wheel operative on the right side. Additional problems were encountered when the left middle wheel on the passive bogie suspension was raised off the ground because of unbalanced torques generated by the other wheels. From sols 2078 to 2142 twenty-one drives in the forward direction produced only a few centimeters of lateral motion.

[31] The breakthrough for extrication was the decision to perform wheel “wiggles” for the outer wheels before each drive segment. Wiggles consisted of using the steering actuators to rotate the outer wheels periodically during drives. This action emulated blades plowing through the soil around the wheels and lowered the local compaction and bulldozing resistance. Accordingly, Spirit made 34 cm of progress during its last set of ten backward drives from sols 2145 to 2165 that included wheel wiggles. In addition, the left front wheel produced a set of sand “waves” and excavated additional bright soils during these last drives (Figures 22–23). After

the sol 2169 drive a stand down was called in order to prepare Spirit for the winter, with the expectation that drives would continue when solar energy became high enough during the ensuing spring to resume activities. Vehicle yaw, pitch, and roll just after the last drive on sol 2165 was 310, –4, and 16° respectively, with a 9° southerly tilt.

8. Pedogenic History

[32] The left side wheels excavated more bright soil within Scamander crater during Spirit’s final 34 cm of backward drives (see Figure 11). The dragging of the right front wheel, on the other hand, did not excavate bright material. Spirit was sitting on the side of Scamander crater before extrication and the rearward drives kept the left wheels within the crater. This indicates that Scamander has been in-filled by a mix of ferric sulfate and basaltic materials. The Pancam false color mosaic generated after Spirit stopped for the winter (Figure 23) shows a red layer to either side of the sulfate-rich disturbed soils, extending onto the floor of Scamander crater. The appearance of this material is similar to that of the red layer found near C. L. Moore (Figure 4) and a search of Pancam color data for Arad and Tyrone sulfate soils exposed by wheel motions also suggests the presence of a red layer.

[33] The shallow subsurface crusty soils exposed on the eastern Ulysses cliff are enriched in hematite and ferric sulfate, and perhaps calcium sulfate and silica, relative to the bulk of the ferric sulfate and basaltic materials. The origin of the sulfate and silica-rich materials in the Inner Basin in association with fumarole and/or hydrothermal acid-sulfate aqueous environments has been discussed in detail by *Yen*

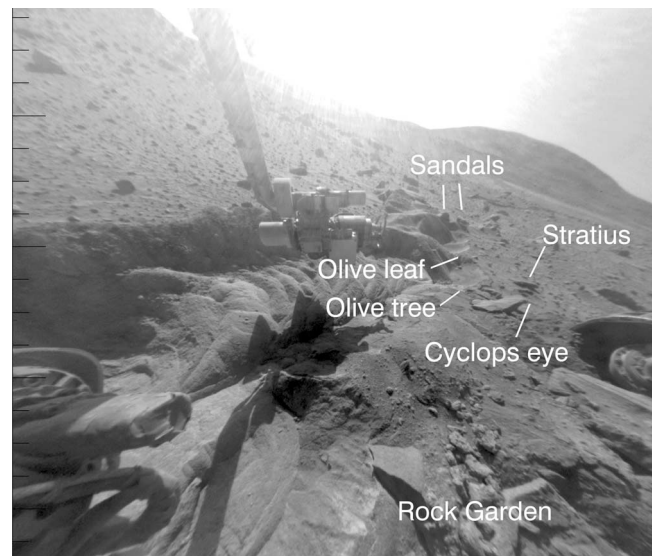


Figure 22. Front Hazcam image taken on sol 2169 after Spirit’s backward extrication maneuvers ceased because of decreasing energy availability due to the onset of the winter season. The last set of ten drives produced 34 cm of motion, with additional excavation of material in Scamander crater by the left front wheel, and exposure of part of the Rock garden. Key targets are labeled. Frame 2F318929944RALB27MP1214L0M1.

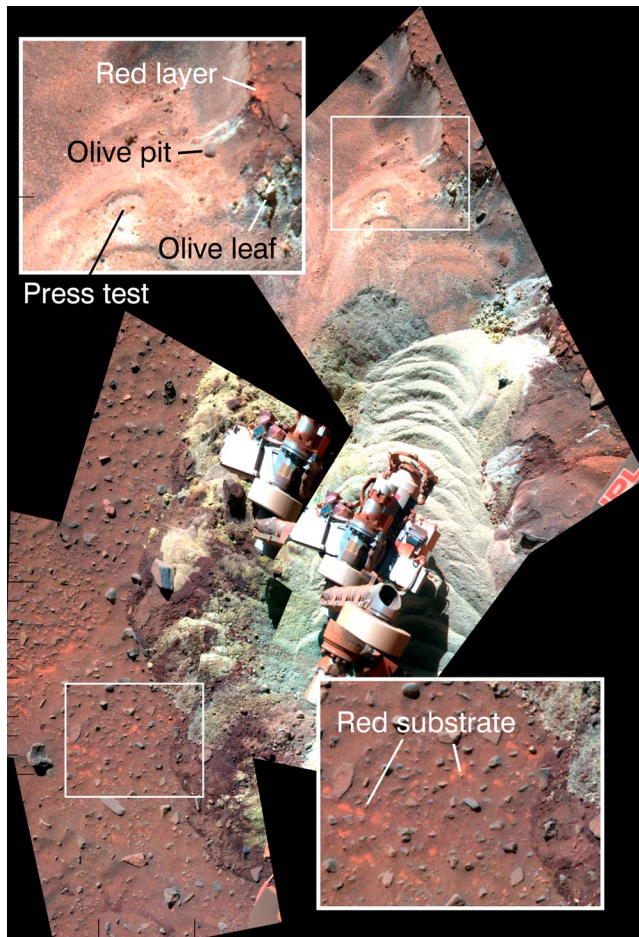


Figure 23. Pancam false color mosaic from sols 2163 and 2177 showing Ulysses disturbed soils excavated during the last ten backward extrication drives. Note “sand waves” excavated by the left front wheel. The brightness and color indicate that these newly exposed deposits are also sulfate-rich, providing further evidence that the floor of Scamander crater is underlain by these materials. Key targets are shown, including the location of a press test where the RAT was used to determine soil deformation as a function of applied normal stress. Note the white soil exposed on the cliffs to the right of the newly excavated soils. The original Ulysses area acquired a reddish color (e.g., compare to sol 1933 Pancam data, Figure 12), presumably due to dust deposition. The IDD instruments block part of the newly excavated soil exposures.

et al. [2008], *Wang et al.* [2008], *Squyres et al.* [2008], and S. Ruff *et al.* (manuscript in preparation, 2010), and will not be addressed in this paper. Rather, the focus is on the processing of these materials after mixing with basaltic materials and accumulation within Scamander crater. The most likely explanation for the occurrence of ferric sulfates and basaltic sands within the crater is that these minerals were transported from other locations within the Inner Basin and accumulated as aeolian deposits. Alternately they might be primary fumarole or hydrothermal deposits. In any case the data indicate that ongoing pedogenic processes have modified these materials since their emplacement.

[34] The addition of neutral to slightly acidic water to material containing ferric sulfate minerals would result in preferential ferric sulfate dissolution, iron oxide formation (nominally as hematite), and generation of a sulfuric acid-rich fluid (Figure 24). Coexisting basaltic materials would also be unstable in such fluids, as exemplified by their increasing solubility with decreasing pH (Figure 24). On the other hand dissolution rates of basaltic materials would be slow as compared to dissolution rates for ferric sulfates [Brantley, 2008]. Competing with these dissolution reactions would be the downward migration of the acidic fluid driven by gravity and/or diffusion, which would be subsequently followed by sublimation or freezing. Provided that the acidic fluid was not fully neutralized by reaction with basaltic materials, the freezing or sublimation of this fluid would result in the redeposition of ferric sulfates, forming layers enriched in this material. Given the expected temperature and pressure conditions, the latter process likely occurred substantially faster than neutralization by reaction with basaltic components.

[35] Thus it is postulated that neutral to slightly acidic water has been added episodically to the soils in the valleys surrounding Home Plate. Aqueous solution then migrated into the subsurface, ultimately leaving behind relatively insoluble species close to the surface and ferric sulfate-enriched layers perhaps just centimeters beneath the surface. The observation that the sulfate-rich deposits and the surface crusts follow the topography is an important clue for understanding the time scale associated with the evolution of these deposits. It implies that the dissolution and reprecipitation must have been ongoing processes because the landforms in the Inner Basin have continually evolved due to aeolian

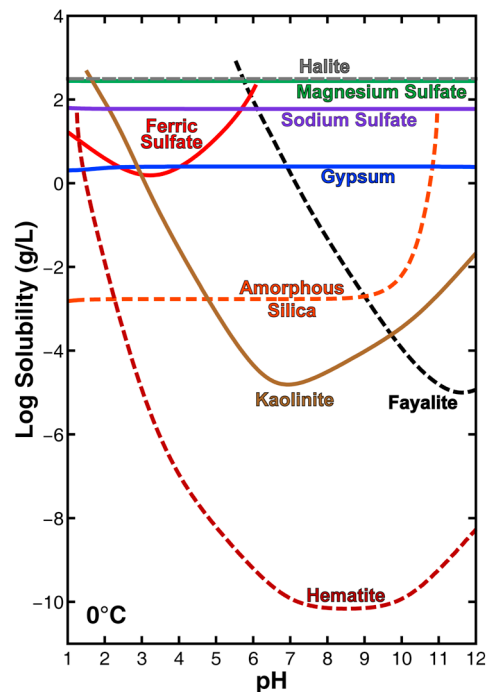


Figure 24. The pH-dependent solubility of site-relevant mineral phases. See Appendix A for details regarding the solubility calculations and text for explanation.

erosion and deposition [e.g., *Grant et al.*, 2006]. We postulate that production of thin films of water associated with frost formation and snowpack development, e.g., during periods of high obliquity, have provided the necessary small amounts of water. Reactions have not gone to completion because basaltic minerals persist in the crusts and sands of Troy and have not reacted completely with the ferric sulfates.

9. Conclusions and Implications

[36] Spirit spent its third winter on the northern slopes of Home Plate. During the ensuing spring season the rover drove down onto the valley to the north of Home Plate on its way south to investigate von Braun and Goddard. An initial target consisted of nodular rock that was found to be composed primarily of silica. With its limited five-wheel drive capability Spirit was unable to get clockwise around the northeastern side of Home Plate or counterclockwise using the valley to the west of Home Plate. Drives on soil-covered slopes proved to be particularly problematical and led to significant slippage, sinkage, and excavation of subsurface soils. This ultimately led to embedding in the sands of Troy in the valley to the west of Home Plate. On the other hand, the excavated soils were found to be enriched in ferric sulfate-bearing materials located only centimeters beneath crusty surface layers enriched in these salts together with iron oxides, calcium sulfate, and silica. The valleys around Home Plate are thus special places in which soils contain substantial deposits of highly soluble ferric sulfate materials of likely fumarole or hydrothermal origin that have been processed by ongoing aqueous processes to form thin crusts overlying mixtures of sulfate-rich and basaltic sands. These areas are intrinsically interesting but also hazardous for driving a mobility-impaired vehicle.

[37] On Earth fumaroles and hydrothermal systems provide the environmental conditions, water, nutrients and energy sources needed to sustain robust microbial communities [*Walter and Des Marais*, 1993]. For example, despite their acidity, iron-rich sulfate hot springs in Yellowstone National Park support thriving microbial communities [*Innskeep and McDermott*, 2005]. Spirit has shown that deposits rich in silica and/or ferric sulfates of likely fumarole or hydrothermal origins occur along most, if not all, of the perimeter of Home Plate. It seems likely that the region in and around Home Plate may have likewise supported a habitable environment. Whether habitable environments accompanied the more recent aqueous activity that redistributed the near-surface ferric sulfate salts at Troy is less certain. The water activities of solutions saturated in ferric sulfate may have been too low to maintain microbial metabolism [e.g., *Tosca et al.*, 2008]. Thus the near-surface transient brines that redistributed ferric sulfate in the sands of Troy probably did not sustain habitable conditions.

Appendix A

[38] Calculations were performed using The Geochemist's Workbench® [*Bethke*, 2009]. The Lawrence Livermore National Laboratory thermochemical database [*Delany and Lundeen*, 1990] was employed with additional mineral solubility constants at 0°C obtained from the compilation by *Marion et al.* [2008]. An extended Debye–Huckel activity

correction model was employed that is parameterized to be accurate in up to 3 m NaCl solution and approximately 0.5–1 m ionic strengths of other electrolytes [*Helgeson*, 1969; *Helgeson and Kirkham*, 1974a, 1974b]. The solubilities of the most soluble phases (magnesium sulfate, halite, ferric sulfate, gypsum, sodium sulfate) were calculated using the extension of the thermochemical database of *Harvie et al.* [1984] by *Tosca et al.* [2008], which employs a Pitzer-type activity model to account for the effect of high ionic strength solutions. Hematite solubility was also calculated in this model to establish a relatively accurate intersection with the ferric sulfate solubility curve. The main hydrolysis species of iron were added to the *Tosca et al.* [2008] model for this purpose.

[39] Mineral solubilities as a function of pH were calculated by first equilibrating the mineral phase with pure water and then titrating the system using Ca(OH)₂ or H₂SO₄. These species were chosen to reflect a Ca-SO₄ electrolyte that should dominate at the site in question. Except at extreme pH values the solubility curves are generally independent of electrolyte concentration and composition as the activity corrections and complexation by Ca²⁺ and SO₄²⁻ were minimal for the species considered. The more soluble phases were titrated to high pH using the mineral cation to prevent supersaturation with respect to gypsum or anhydrite.

[40] It is acknowledged that quantitative solubility calculations are system dependent because of activity corrections, common ion effects, and complexation. However, the purpose of the diagram shown in Figure 24 was not to produce solubility curves to be employed directly in quantitative chemical models. Rather, these calculations are intended to illustrate how the solubilities of key minerals at this site can differ by more than 13 orders of magnitude and also vary substantially as a function of pH. Because system-specific effects typically modify individual values by only an order of magnitude or less, the larger differences shown in relative solubilities displayed in Figure 24 illustrate the potential consequences of aqueous processes in these deposits.

[41] **Acknowledgments.** We thank the capable team of engineers and scientists at the Jet Propulsion Laboratory and elsewhere who made the Spirit mission possible. We also thank support from NASA for the science team.

References

- Arvidson, R. E., et al. (2004), Localization and physical properties experiments conducted by Spirit at Gusev crater, *Science*, *305*, 821–824, doi:10.1126/science.1099922.
- Arvidson, R. E., et al. (2006), Overview of the Spirit Mars Exploration Rover Mission to Gusev Crater: Landing site to Backstay Rock in the Columbia Hills, *J. Geophys. Res.*, *111*, E02S01, doi:10.1029/2005JE002499.
- Arvidson, R. E., et al. (2008), Spirit Mars Rover Mission to the Columbia Hills, Gusev Crater: Mission overview and selected results from the Cumberland Ridge to Home Plate, *J. Geophys. Res.*, *113*, E12S33, doi:10.1029/2008JE003183.
- Bekker, M. G. (1969), *Introduction to Terrain-Vehicle Systems*, Univ. of Mich. Press, Ann Arbor.
- Bell, J. F., III, et al. (2003), Mars Exploration Rover Athena Panoramic Camera (Pancam) investigation, *J. Geophys. Res.*, *108*(E12), 8063, doi:10.1029/2003JE002070.
- Bell, J. F., III, et al. (2006), In-flight calibration and performance of the Mars Exploration Rover Panoramic Camera (Pancam) Instruments, *J. Geophys. Res.*, *111*, E02S03, doi:10.1029/2005JE002444.
- Bethke, C. M. (2009), *The Geochemist's Workbench Release 8.0*, Hydrogeol. Program, Univ. of Ill., Urbana.

- Brantley, S. L. (2008), Kinetics of mineral dissolution, in *Kinetics of Water-Rock Interaction*, edited by S. L. Brantley, J. D. Kubicki, and A. F. White, pp. 151–210, Springer, New York, doi:10.1007/978-0-387-73563-4_5.
- Campbell, J. L., R. Gellert, M. Lee, C. L. Mallett, J. A. Maxwell, and J. M. O'Meara (2008), Quantitative in situ determination of hydration of bright high-sulfate Martian soils, *J. Geophys. Res.*, *113*, E06S11, doi:10.1029/2007JE002959.
- Delany, J. M., and S. R. Lundeen (1990), The LLNL thermochemical database, *Rep. UCRL-21658*, Lawrence Livermore Natl. Lab., Livermore, Calif.
- Gellert, R., et al. (2006), Alpha Particle X-Ray Spectrometer (APXS): Results from Gusev crater and calibration report, *J. Geophys. Res.*, *111*, E02S05, doi:10.1029/2005JE002555.
- Grant, J. A., et al. (2006), Crater gradation in Gusev crater and Meridiani Planum, Mars, *J. Geophys. Res.*, *111*, E02S08, doi:10.1029/2005JE002465.
- Harvie, C. F., N. Møller, and J. H. Weare (1984), The prediction of mineral solubilities in natural waters: The Na-K-Mg-Ca-H-Cl-SO₄-OH-HCO₃-CO₃-CO₂-H₂O system to high ionic strengths at 25°C, *Geochim. Cosmochim. Acta*, *48*, 723–751, doi:10.1016/0016-7037(84)90098-X.
- Helgeson, H. C. (1969), Thermodynamics of hydrothermal systems at elevated temperatures and pressures, *Am. J. Sci.*, *267*, 729–804.
- Helgeson, H. C., and D. H. Kirkham (1974a), Theoretical prediction of thermodynamic behavior of aqueous electrolytes at high pressures and temperatures. 1. Summary of thermodynamic-electrostatic properties of solvent, *Am. J. Sci.*, *274*, 1089–1198.
- Helgeson, H. C., and D. H. Kirkham (1974b), Theoretical prediction of thermodynamic behavior of aqueous electrolytes at high pressures and temperatures. 2. Debye-Hückel parameters for activity-coefficients and relative partial molal properties, *Am. J. Sci.*, *274*, 1199–1261.
- Innskeep, W. P., and T. R. McDermott (2005), Geomicrobiology of acid-sulfate-chloride springs in Yellowstone National Park, in *Geothermal Biology and Geochemistry in Yellowstone National Park*, edited by W. P. Innskeep and T. R. McDermott, pp. 142–162, Montana State Univ., Bozeman.
- Johnson, J. R., J. F. Bell III, E. Cloutis, M. Staid, W. H. Farrand, T. McCoy, M. Rice, A. Wang, and A. Yen (2007), Mineralogic constraints on sulfur-rich soils from Pancam spectra at Gusev crater, Mars, *Geophys. Res. Lett.*, *34*, L13202, doi:10.1029/2007GL029894.
- Lane, M. D., J. L. Bishop, M. D. Dyar, P. L. King, M. Parente, and B. C. Hyde (2008), Mineralogy of the Paso Robles soils on Mars, *Am. Mineral.*, *93*, 728–739, doi:10.2138/am.2008.2757.
- Larsen, K. W., et al. (2000), Correspondence and least squares analyses of soil and rock compositions for the Viking Lander 1 and Pathfinder landing sites, *J. Geophys. Res.*, *105*(E12)29,207–29,221, doi:10.1029/2000JE001245.
- Lewis, D. W., and D. McConchie (1994), *Analytical Sedimentology*, 197 pp., Chapman and Hall, New York.
- Lindemann, R. A., and C. J. Voorhees (2005), Mars Exploration Rover mobility assembly design, test and performance, *IEEE Int. Conf. Syst., Man and Cybern.*, *1*, 450–455, doi:10.1109/ICSMC.2005.1571187.
- Ling, Z. C., A. Wang, and C. Li (2009), Comparative spectroscopic study of three ferric sulfates: Kornelite, lausenite and pentahydrate, *Lunar Planet. Sci.*, *XL*, Abstract 1867.
- Maimone, M., Y. Cheng, and L. Matthies (2007), Two years of visual odometry on the Mars Exploration Rovers, *J. Field Robot.*, *24*(3), 169–186, doi:10.1002/rob.20184.
- Marion, G. M., J. S. Kargel, and D. C. Catling (2008), Modeling ferrous-ferric iron chemistry with application to Martian surface geochemistry, *Geochim. Cosmochim. Acta*, *72*, 242–266, doi:10.1016/j.gca.2007.10.012.
- Rice, M. S., J. F. Bell III, E. A. Cloutis, A. Wang, S. Ruff, M. A. Craig, D. T. Bailey, J. R. Johnson, P. A. de Souza Jr., and W. H. Farrand (2010), Silica-rich deposits and hydrated minerals at Gusev Crater, Mars: Vis-NIR spectral characterization and regional mapping, *Icarus*, *205*, 375–395, doi:10.1016/j.icarus.2009.03.035.
- Richter, L., et al. (2006), A predictive wheel-soil interaction model for planetary rovers validated in testbeds and against MER Mars rover performance data, paper presented at 10th European Conference of the International Society for Terrain-Vehicle Systems, Budapest, Hungary, 3–6 Oct.
- Siebach, K. (2010), Recent Spirit results: Microscopic Imager analysis of particle properties in Scamander crater, west of Home Plate, *Lunar Planet. Sci.*, *XLI*, Abstract 2548.
- Squyres, S. W., R. E. Arvidson, S. Ruff, R. Gellert, R. V. Morris, D. W. Ming, L. S. Crumpler, J. D. Farmer, D. J. Des Marais, and P. A. de Souza (2008), Detection of silica-rich deposits on Mars, *Science*, *320*, 1063–1067, doi:10.1126/science.1155429.
- Tosca, N. J., A. H. Knoll, and S. M. McLennan (2008), Water activity and the challenge for life on early Mars, *Science*, *320*, 1204–1207, doi:10.1126/science.1155432.
- Walter, M. R., and D. J. Des Marais (1993), Preservation of biological information in thermal spring deposits: Developing a strategy for the search for fossil life on Mars, *Icarus*, *101*, 129–143, doi:10.1006/icar.1993.1011.
- Wang, A., et al. (2008), Light-toned salty soils and coexisting Si-rich species discovered by the Mars Exploration Rover Spirit in Columbia Hills, *J. Geophys. Res.*, *113*, E12S40, doi:10.1029/2008JE003126.
- Wong, J. (2003), *Theory of Ground Vehicles*, 2nd ed., John Wiley, New York.
- Yen, A. S., et al. (2008), Hydrothermal processes at Gusev Crater: An evaluation of Paso Robles class soils, *J. Geophys. Res.*, *113*, E06S10, doi:10.1029/2007JE002978.
- R. E. Arvidson, J. G. Catalano, R. N. Greenberger, E. A. Guinness, K. A. Lichtenberg, A. Shaw, K. L. Siebach, and A. Wang, Department of Earth and Planetary Sciences, Washington University in St. Louis, St. Louis, MO 63130, USA. (arvidson@rsmail.wustl.edu)
- J. F. Bell III, M. S. Rice, S. W. Squyres, and R. J. Sullivan, Department of Astronomy, Cornell University, Ithaca, NY 14853, USA.
- P. Bellutta, T. A. Estlin, J. A. Herman, S. A. Maxwell, A. W. Stroupe, K. P. Talley, J. A. Townsend, J. R. Wright, and A. S. Yen, Jet Propulsion Laboratory, California Institute of Technology, Pasadena, CA 91125, USA.
- N. A. Cabrol and D. J. Des Marais, NASA Ames Research Center, Moffett Field, CA 94035, USA.
- J. Cohen, Honeybee Robotics Spacecraft Mechanisms Corporation, 460 West 34th St., New York, NY 10001, USA.
- L. S. Crumpler, New Mexico Museum of Natural History and Science, 1801 Mountain Rd. NW, Albuquerque, NM 87104, USA.
- P. A. de Souza, Information and Communication Technologies Centre, CSIRO, Hobart, Tas 7001, Australia.
- W. H. Farrand, Space Science Institute, 4750 Walnut St., Boulder, CO 80301, USA.
- R. Gellert, Department of Physics, University of Guelph, Guelph, ON N1G 2W1, Canada.
- J. A. Grant, Center for Earth and Planetary Studies, Smithsonian Institution, PO Box 37012, Washington, DC 20013, USA.
- K. E. Herkenhoff and J. R. Johnson, U.S. Geological Survey, 2255 North Gemini Dr., Flagstaff, AZ 86001, USA.
- K. D. Iagnemma, Department of Mechanical Engineering, Massachusetts Institute of Technology, Cambridge, MA 02139, USA.
- G. Klingelhöfer, Institut für Anorganische und Analytische Chemie, Johannes Gutenberg-Universität, Mainz D-55099, Germany.
- R. Li, Department of Civil and Environmental Engineering and Geodetic Science, Ohio State University, Columbus, OH 43210, USA.
- D. W. Ming and R. V. Morris, NASA Johnson Space Center, Houston, TX 77058, USA.
- S. W. Ruff, School of Earth and Space Exploration, Arizona State University, Tempe, AZ 85287, USA.